University of Crete
Physics Department

Enhanced optical cross section, superradiance and subradiance from strongly interacting atoms

Filippos Tzimkas-Dakis

Master Thesis

Heraklion, June 2022

Enhanced optical cross section, superradiance and subradiance from strongly interacting atoms

SUPERVISOR

David Petrosyan
Principal Researcher IESL-FORTH

MASTER THESIS COMMITTEE

David Petrosyan	Principal Researcher
Ioannis Kominis	Professor
Konstantinos Makris	Professor

Η έγκριση της παρούσας Μεταπτυχιακής Εργασίας από το Τμήμα Φυσικής του Πανεπιστημίου Κρητης δεν υποδηλώνει αποδοχή των γνωμών του συγγραφέα (Ν. 5343/1932, άρθρο 202, παρ. 2)

Dedicated to my mother and my father.

Περιληψη

Η μεταπτυχιακή εργασία εντάσεται στην ευρύτερη περιοχή της Κβαντικής Οπτικής. Το αντικείμενο εξειδικεύτεται στις ιδιότητες ακτινοβολίας ατομικών συλλογών, με διατομικές αποστάσεις μικρότερες του μήκους κύματος, που οδηγούνται από σύμφωνη ακτινοβολία laser και αλληλεπιδρούν έντονα μεταξύ τους μέσω της αλληλεπίδρασης δίπολου-διπόλου στον ελεύθερο χώρο. Μελετάμε μεγάλα διδιάστατα πετάσματα ατόμων υπό την προσέγγιση της μονής διέγερσης διερευνώντας τη συλλογική τους συμπεριφορά που οδηγεί στην ενισχυμένη διατομή σκέδασης. Επιπλεόν, προτείνουμε τρόπους εκμετάλλευσης της συλλογικής απόκρισης για τη δημιουργία κατόπτρων, φακών και εκτροπέων για ασθενείς δέσμες φωτός. Αναπτύξαμε μια αριθμητική μέθοδο για να περιγράψουμε αποτελεσματικά το σύστημα διάχυσης πολλών σωμάτων των ατόμων που βρίσκονται σε κοντινή απόσταση χρησιμοποιώντας μια προσέγγιση στοχαστικής κυματοσυνάρτησης Monte-Carlo προσαρμοσμένη να εξηγεί τη συνεργατική αποδιέγερση των πολλαπλά διεγερμένων ατομικών συστημάτων. Εφαρμόζουμε αυτή τη μέθοδο σε ποικίλες γεωμετρίες ατόμων διότι μας επιτρέπει να μελετάμε την εκπομπή υπερακτινοβολίας και υποακτινοβολίας των φωτονίων και να υπολογίζουμε τις συσχετίσεις τους αποκαλύπτοντας τη συσσώρευση (bunching) και την αντισυσσώρευση (antibunching) φωτονίων. Για την καλύτερη κατανόηση των φασμάτων διέγερσης του συστήματος καθώς και των συσχετίσεων μεταξύ των εκπεμπόμενων φωτονίων, διαγωνοποιούμε την μη-Ερμητιανή Χαμιλτονιανή του συστήματος και εξάγουμε τις διάφορες διαδρομές διέγερσης και συλλογικής αποδιέγερσης που εξερευνά το σύστημα κάτω από συνεχή ακτινοβολία (continuous wave) laser. Η παρούσα μελέτη ειναι επίκαιρη και σχετική με την πρόσφατη αναζήτηση περιοδικών συστοιχιών ατόμων που χρησιμεύουν ως οπτικές κεραίες (optical antennas) με ιδιαίτερα χρήσιμες ιδιότητες, συμπεριλαμβανομένης της εξαιρετικά αποτελεσματικής και κατευθυντικής εκπομπής, απορρόφησης και ανάκλασης φωτονίων. Με σκοπό να προχωρήσουμε πέρα από τις προηγούμενες μελέτες δεν περιορίζουμε τον χώρο Hilbert του συστήματος σε μία ή λίγες διεγέρσεις, γεγονός που μας επιτρέπει να αποκαλύψουμε τη μη-γραμμική συμπεριφορά της αλληλεπίδρασης ατόμου-φωτός.

Abstract

This thesis lies in the broader area of Quantum Optics. The subject focuses in the radiation properties of atomic ensembles with subwavelength interatomic distances driven by coherent laser radiation and strongly interacting with each other via the free-space dipole-dipole interaction. We study large two-dimensional arrays of atoms under the single excitation approximation, exploring their collective behavior with enhanced effective cross section for interaction with light. We then suggest ways of exploiting collective atomic response to create mirrors, lenses and deflectors for weak beams of light. We developed a numerical method to efficiently describe the many-body dissipative system of closely-spaced atoms using a Monte-Carlo stochastic wavefunction approach adapted to account for cooperative decay of multiply-excited states of the system. We apply this method to various geometries of atomic positions in order to study superradiant and subradiant emission of the photons and calculate their correlations revealing the photon bunching and anti-bunching. To better understand the laser-excitation spectrum of the system and the correlations of the emitted photons, we diagonalize the effective non-Hermitian Hamiltonian and deduce the various excitation and collective decay paths that the system explores during the continuous driving. Our studies are relevant to the recent quest to tailor the cooperative radiative properties of periodic arrays of atoms serving as phased-array optical antennas with unique properties, including the highly efficient and directional photon emission, absorption and reflection. But in order to go beyond the previous studies, we do not truncate the Hilbert space of the system to a single or a few-excitation sub-space, which permits us to reveal the non-linear regime of the cooperative atom-light interaction.

Preface

This thesis is the result of my study and research in the field of Quantum Optics during the last year of my Master's degree at the Physics Department of University of Crete. At this point, I would like to thank my supervisor Dr. David Petrosyan, Principal Researcher at IESL-FORTH, for giving me the opportunity to collaborate with him in the challenging field of Quantum Optics, for carefully guiding me throughout this project, and for always being there to answer my questions and discuss new ideas.

I want to thank my friend and colleague Michalis Koutrakis for sharing the same office the last two years, and for having valuable scientific and general discussions. Also, I thank my friend Konstantinos Kontogeorgiou for always being eager to discuss scientific stuff, and for his constantly positive attitude.

I could not omit to express my sincere gratitude to Bodossakis Foundation for granting me a scholarship for my Master's degree. The scholarship along with the very supportive staff of the Foundation motivated me to focus on my studies and overcome any obstacle towards achieving my goals.

Finally, I am totally grateful to Dimitra and my family for their unwavering support and faith in my choices.

"*Δεν φταίει το σχολείο για όσα μπόρεσα,*
φταίει που πεινούσα και δεν χόρτασα ..."

– Αλέξης Λαναράς

Filippos Tzimkas-Dakis
Heraklion, June 2022

Contents

Page

1 Introduction **1**

2 Theoretical Framework **3**
2.1 Derivation of Master Equation 3
2.1.1 Analytical solution for interacting pair of atoms 7
2.2 Quantum Stochastic Wavefunction Monte-Carlo 10
2.2.1 Spontaneous decay of a two-level atom 13
2.2.2 Driven two-level atom 14
2.2.3 Ensemble of interacting atoms 16
2.2.3.1 Numerical solutions for a pair of atoms 17

3 Enhanced Optical Cross Section **21**
3.1 Single excitation approximation 21
3.1.1 Atoms 21
3.1.2 Incoming beam 22
3.1.3 Radiated field 23
3.2 Collective response of spatially-periodic atomic ensembles 24
3.2.1 Single dipole 24
3.2.2 Many interacting dipoles 24
3.2.2.1 Ordered arrays of atoms 26
3.2.2.2 Inhomogeneous atomic arrays 29
3.2.3 Pulsed fields 32

4 Multiple Excitations **35**
4.1 Pair of atoms 35
4.2 Three atoms 42
4.2.1 Chain configuration 42
4.2.2 Triangle configuration 44

5 Conclusions and Future Extensions **47**

Appendix A Detection of selected mode **49**

Chapter 1

Introduction

Superradiance and subradiance have been an active topic of research since the seminal paper of Dicke [1] on collective emission of atoms confined within a distance that is small compared to the wavelength of the resonantly emitted radiation. The behavior of the single and multiple-excitation states of the interacting atoms can be understood in terms of the collective eigenstates of an effective non-Hermitian Hamiltonian [2, 3], which exhibit enhanced (superradiant) and suppressed (subradiant) decay rates, together with level shifts (collective Lamb shift) [4]. Recent experiments have demonstrated both subradiance [5, 6] and superradiance [7] in large, dilute atomic clouds.

The present thesis deals with collection of atoms which interact with each other through the free radiation field modes. This coupling affects the way the atomic ensemble can be excited and how they decay by radiating photons exhibiting superradiance and subradiance phenomena [1]. Although there has been an extended research on the collective single-excitation states of the spatially-periodic atomic ensembles [8–11], much less has been done for the multiple excited states, which is one of the main purposes of this project. The second purpose is to investigate further the singly-excited subwavelength atomic arrays in order to explain their behavior as perfect mirrors for the incoming photons. We also take advantage of the cooperative enhancement of the light–matter coupling [12] and explore the possibilities to focus and deflect an incoming photon mode by two-dimensional periodic arrays of atoms.

In chapter two we present the mathematical framework to describe the quantum interactions between N cold atoms at random positions and the quantized radiation field mediating interatomic interactions and their collective behavior. We derive the master equation for the reduced density matrix of the atomic system, and we introduce the Quantum Stochastic Wavefunction Monte–Carlo method and apply it to our problem.

In chapter three we consider singly-excited atomic ensembles and study the atomic response to a weak incident laser beam. We reveal the ability of periodic subwavelength arrays to achieve enhanced optical cross section and suggest ways to increase it further by applying spatially modulated detuning of the atoms in the array. We also propose detuning profiles that result in focusing and deflection of the incoming photon beams.

In chapter four we investigate small ensembles of closely-spaced atoms by looking at their eigenvalue spectrum, emission rate spectra, and excitations in the system. We calculate the second order correlation function of the radiated photons revealing photon bunching and anti-bunching.

Finally, in chapter five we summarize the conclusions of the last two chapters and discuss possible future extensions of this work.

Chapter 2

Theoretical Framework

The purpose of this chapter is to set the appropriate theoretical and mathematical foundations to describe the superradiant and subradiant phenomena in ensembles of interacting atoms. In the first section we derive the Master Equation (ME) for the reduced density matrix for an ensemble of atoms. In the second section, we present the Quantum Stochastic Wavefunction (QSW) Monte-Carlo method for the simple case of an isolated atom driven by classical field. We the derive the QSW Monte-Carlo method for an ensemble of atoms and compare the results with those obtained from ME for the case of two closely spaced atoms.

2.1 Derivation of Master Equation

Consider a collection of N identical nonoverlapping atoms at positions $\boldsymbol{r}_1, \boldsymbol{r}_2, ...\boldsymbol{r}_N$ coupled to the free-space quantized electromagnetic field $\hat{\boldsymbol{E}}(\boldsymbol{r}) = \sum_{\boldsymbol{k}} \hat{a}_{\boldsymbol{k}} \boldsymbol{u}_{\boldsymbol{k}}(\boldsymbol{r})$, where $\hat{a}_{\boldsymbol{k}}$ ($\hat{a}^\dagger_{\boldsymbol{k}}$) are the bosonic annihilation (creation) operators for the plane-wave mode

$$\boldsymbol{u}_{\boldsymbol{k}}(\boldsymbol{r}) = \hat{\mathbf{e}}_{\boldsymbol{k},\nu} \sqrt{\frac{\hbar\omega_{\boldsymbol{k}}}{2\epsilon_0 V}}\, e^{i\boldsymbol{k}\cdot\boldsymbol{r}}\,, \tag{2.1}$$

where $\boldsymbol{k}$ is the wave vector, $\hat{\mathbf{e}}_{\boldsymbol{k},\nu}$ are the polarization unit vectors ($\nu = 1, 2$), $\omega_{\boldsymbol{k}}$ is the frequency, and ϵ_0 is the vacuum permittivity. Note that these modes form a complete basis for the field within the quantization volume V. Each atom is assumed to have only two relevant energy states[1], the excited $|e\rangle$ and the ground state $|g\rangle$. The Hamiltonian of the system is

$$\begin{aligned}
\mathcal{H} &= \mathcal{H}_{Field} + \mathcal{H}_{System} + \mathcal{V} \\
&= \sum_{\boldsymbol{k}} \hbar\omega_{\boldsymbol{k}} \hat{a}^\dagger_{\boldsymbol{k}} \hat{a}_{\boldsymbol{k}} + \sum_{j=1}^{N} \sum_{\mu=g,e} \hbar\omega_\mu \left|\mu\right\rangle_j \langle\mu| - \sum_{j=1}^{N} \boldsymbol{\mathcal{E}}(\boldsymbol{r}_j, t) \cdot \left(\wp \left|e\right\rangle_j \langle g| + \wp^* \left|g\right\rangle_j \langle e|\right) \\
&- \sum_{j=1}^{N} \left(\hat{\boldsymbol{E}}(\boldsymbol{r}_j) + \hat{\boldsymbol{E}}^\dagger(\boldsymbol{r}_j)\right) \cdot \left(\wp \left|e\right\rangle_j \langle g| + \wp^* \left|g\right\rangle_j \langle e|\right),
\end{aligned} \tag{2.2}$$

where the first term on the right-hand side is the Hamiltonian for the field modes with energies $\hbar\omega_{\boldsymbol{k}}$, the second term (double summation) corresponds to the energies $\hbar\omega_\mu$ of the atomic levels $|e\rangle$ and $|g\rangle$, the third term represents the interaction of the atoms at positions $\boldsymbol{r}_j$

[1] For this reason we may also refer to atoms as Two-Level Systems (TLS).

with the classical driving laser, and the last term describes the coupling of the atoms to the quantized free-space radiation field, within dipole approximation, with the dipole moment $\wp$ on the transition $|e\rangle \rightarrow |g\rangle$. The classical field is assumed to be polarized along the direction $\hat{\mathbf{e}}$ and its amplitude is

$$\boldsymbol{\mathcal{E}}(\boldsymbol{r},t) = \hat{\mathbf{e}}\mathcal{E}(\boldsymbol{r})e^{-i\omega_c t} + \hat{\mathbf{e}}^*\mathcal{E}^*(\boldsymbol{r})e^{i\omega_c t}\,, \tag{2.3}$$

with frequency $\omega_{\rm c}$ and wave vector $\boldsymbol{k}_{\rm c} = \hat{\boldsymbol{n}}\omega_c/c$ (where $\hat{\boldsymbol{n}}\cdot\hat{\boldsymbol{e}} = 0$). Without loss of generality, we can set the atomic ground state energy as $\hbar\omega_g = 0$.

Equation (2.2) is our starting point. The next step is to write and solve the equation of motion for the bosonic annihilation (or creation) operators of the field. Namely, from the Heisenberg equation of motion we have

$$\begin{aligned} i\hbar\frac{\partial\hat{a}_{\boldsymbol{k}}}{\partial t} &= [\hat{a_{\boldsymbol{k}}},\mathcal{H}] \Longrightarrow \\ \frac{\partial\hat{a}_{\boldsymbol{k}}}{\partial t} &= -i\omega_{\boldsymbol{k}}\hat{a}_{\boldsymbol{k}}(t) + \frac{i}{\hbar}\sum_{j=1}^{N}\sqrt{\frac{\hbar\omega_{\boldsymbol{k}}}{2\epsilon_0 V}}\;\hat{\mathbf{e}}_{\boldsymbol{k},\nu}\cdot\wp\left(\hat{\sigma}_j(t)+\hat{\sigma}_j^\dagger(t)\right)e^{i\boldsymbol{k}\cdot\boldsymbol{r}_j}\,, \end{aligned} \tag{2.4}$$

hence

$$\begin{aligned} \hat{a}_{\boldsymbol{k}}(t) &= \hat{a}_{\boldsymbol{k}}(0)e^{-i\omega_{\boldsymbol{k}}t} \\ &\quad + \frac{i}{\hbar}\sum_{j=1}^{N}\sqrt{\frac{\hbar\omega_{\boldsymbol{k}}}{2\epsilon_0 V}}\;\hat{\mathbf{e}}_{\boldsymbol{k},\nu}\cdot\wp\;e^{i\boldsymbol{k}\cdot\boldsymbol{r}_j}\int_0^t \mathrm{d}t'\left(\hat{\sigma}_j(t)+\hat{\sigma}_j^\dagger(t)\right)e^{-\omega_{\boldsymbol{k}}(t-t')} \end{aligned} \tag{2.5}$$

where $\sigma_j^\dagger$,σ_j are the atomic raising and lowering operators, $\hat{\sigma}_j = |g\rangle_j\langle e|$.

Next we write the equation of motion for an arbitrary atomic operator $\hat{Q}(t)$,

$$\begin{aligned} i\hbar\frac{\partial\hat{Q}}{\partial t} &= \left[\hat{Q},\mathcal{H}\right] \Longrightarrow \\ \frac{\partial\hat{Q}}{\partial t} &= i\omega_e\sum_j^N\left[\hat{\sigma}_j^\dagger(t)\hat{\sigma}_j(t),\hat{Q}(t)\right] - \frac{i}{\hbar}\sum_j^N\left[\hat{s}_j(t),\hat{Q}(t)\right]\boldsymbol{\mathcal{E}}(\boldsymbol{r}_j,t)\cdot\wp \\ &\quad - \frac{i}{\hbar}\sum_j^N\left[\hat{s}_j(t),\hat{Q}(t)\right]\hat{\boldsymbol{E}}(\boldsymbol{r}_j)\cdot\wp - \hat{\boldsymbol{E}}^\dagger(\boldsymbol{r}_j)\cdot\wp\left[\hat{Q}(t),\hat{s}_j(t)\right]\,, \end{aligned} \tag{2.6}$$

where $\hat{s}_j(t) = \hat{\sigma}_j^\dagger(t) + \hat{\sigma}_j(t)$. We insert Eq. (2.5) into Eq. (2.6), convert the summation over all bosonic modes to integration through the well known relation

$$\sum_{\boldsymbol{k},\nu}\longrightarrow\frac{V}{(2\pi)^3}\int\mathrm{d}^3k\sum_{\nu=1}^{2} = \frac{V}{(2\pi)^3}\int_0^\infty k^2\mathrm{d}^2k\int_{4\pi}\mathrm{d}\Omega_k\sum_{\nu=1}^{2}\,, \tag{2.7}$$

trace out the bosonic degrees of freedom, and apply the rotating wave approximation (RWA)

[13] and the Weisskopf-Wigner approximation[1] [14] to obtain [15]

$$\begin{aligned}\frac{\partial \hat{Q}}{\partial t} =& -\sum_{j}^{\mathrm{N}} i\Delta\left[\hat{\sigma}_j^\dagger\hat{\sigma}_j,\hat{Q}\right] - \sum_{j}^{N} i\left[\Omega_j e^{i(\boldsymbol{k}_c\cdot\boldsymbol{r}_j)}\hat{\sigma}_j^\dagger + \Omega_j^* e^{-i(\boldsymbol{k}_c\cdot\boldsymbol{r}_j)}\hat{\sigma}_j,\hat{Q}\right] \\ &+ \sum_{i\neq j}^{N} iJ_{ij}\left[\hat{\sigma}_i^\dagger\hat{\sigma}_j,\hat{Q}\right] + \sum_{i,j}^{N}\Gamma_{ij}\left[\hat{\sigma}_i^\dagger\hat{Q}\hat{\sigma}_j - \frac{1}{2}\left(\hat{\sigma}_i^\dagger\hat{\sigma}_j\hat{Q} + \hat{Q}\hat{\sigma}_i^\dagger\hat{\sigma}_j\right)\right],\end{aligned} \tag{2.8}$$

where we introduced the detuning $\Delta = \omega_c - \omega_e$, and the Rabi frequency $\Omega = \boldsymbol{\wp}\cdot\hat{\mathbf{e}}\mathcal{E}/\hbar$. Equation (2.8) is written in the frame rotating with the frequency ω_c of the external classical field $\boldsymbol{\mathcal{E}}$, and we dropped the obvious time-dependence notation for all the atomic operators, i.e. $\hat{\sigma} \equiv \hat{\sigma}(t)$. In Eq. (2.8) the third and forth terms represent the rate of coherent interactions and dissipative interactions between atom i and atom j, respectively, [10] given by

$$-J_{ij} + i(\Gamma_{ij}/2) = \frac{k_e^2}{\hbar\epsilon_0}\boldsymbol{\wp}^*\cdot\overline{\overline{\mathbf{G}}}(\boldsymbol{r}_i,\boldsymbol{r}_j,\omega_e)\cdot\boldsymbol{\wp}\,, \tag{2.9}$$

where the wave number $k_e = 2\pi/\lambda_e$ corresponds to the atomic resonant frequency ω_e, and the Green's tensor $\overline{\overline{\mathbf{G}}}(\boldsymbol{r}_i,\boldsymbol{r}_j,\omega_0)$ is the fundamental solution of of the electromagnetic wave equation[2] [16, 17]

$$\overline{\overline{\mathbf{G}}}(\boldsymbol{r}_i,\boldsymbol{r}_j,\omega_0) = \frac{e^{ik_0r}}{4\pi r}\left[\left(1+\frac{i}{k_0r}-\frac{1}{k_0^2r^2}\right)\overline{\overline{\mathbf{I}}} + \left(-1-\frac{3i}{k_0r}+\frac{3}{k_0^2r^2}\right)\frac{\boldsymbol{r}\otimes\boldsymbol{r}}{r^2}\right], \tag{2.10}$$

with $\overline{\overline{\mathbf{I}}}$ being the unit dyad (unit tensor), and $\boldsymbol{r} = \boldsymbol{r}_i - \boldsymbol{r}_j$. Equation (2.9) can be written in an explicit form as

$$\begin{aligned}\frac{J_{ij}}{\Gamma} = -\frac{3}{4}\Bigg\{&\left[1-(\hat{\boldsymbol{\wp}}\cdot\hat{\boldsymbol{r}}_{ij})^2\right]\frac{\cos(k_er_{ij})}{k_er_{ij}} \\ &-\left[1-3(\hat{\boldsymbol{\wp}}\cdot\hat{\boldsymbol{r}}_{ij})^2\right]\left[\frac{\sin(k_er_{ij})}{(k_er_{ij})^2}+\frac{\cos(k_er_{ij})}{(k_er_{ij})^3}\right]\Bigg\}\end{aligned} \tag{2.11a}$$

$$\begin{aligned}\frac{\Gamma_{ij}}{\Gamma} = \frac{3}{2}\Bigg\{&\left[1-(\hat{\boldsymbol{\wp}}\cdot\hat{\boldsymbol{r}}_{ij})^2\right]\frac{\sin(k_er_{ij})}{k_er_{ij}} \\ &+\left[1-3(\hat{\boldsymbol{\wp}}\cdot\hat{\boldsymbol{r}}_{ij})^2\right]\left[\frac{\cos(k_er_{ij})}{(k_er_{ij})^2}-\frac{\sin(k_er_{ij})}{(k_er_{ij})^3}\right]\Bigg\},\end{aligned} \tag{2.11b}$$

where $\Gamma = \frac{1}{4\pi\epsilon_0}\frac{4k_e^3|\wp_{eg}|^2}{3\hbar}$ is the usual spontaneous decay rate of an isolated atom in excited state [13], $\hat{\boldsymbol{\wp}} \equiv \boldsymbol{\wp}_{eg}/\wp$ is the unit vector in the direction of the atomic dipole moment, $\hat{\boldsymbol{r}}_{ij} \equiv \boldsymbol{r}_{ij}/r_{ij}$ is the unit vector along the direction of the relative position vector $\boldsymbol{r}_{ij} = \boldsymbol{r}_i - \boldsymbol{r}_j$, and $r_{ij} \equiv |\boldsymbol{r}_{ij}|$ is the distance between atoms i and j. In Eq. (2.8), in the summation for Γ's the term $\Gamma_{jj} = \Gamma$, while in the summation of J's we excluded the terms $i = j$ assuming that

[1] It is also known as Born-Markov approximation.

[2] In other words, Green's function describes the electromagnetic field at point $\boldsymbol{r}_i$ produced by a (point) dipole at $\boldsymbol{r}_j$ oscillating with frequency ω_0.

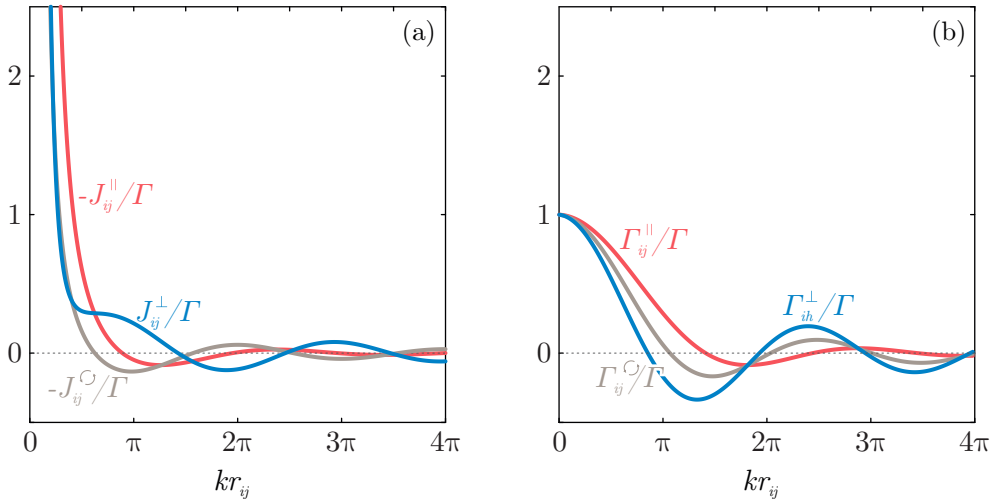

Figure 2.1: Dependence of the dipole-dipole interaction between two atoms on the normalized interatomic distance kr_{ij}. (a) Exchange rates J_{ij} for dipole matrix element $\boldsymbol{\wp}$ parallel (red), perpendicular (blue) and circular (grey) to $\boldsymbol{r}_{ij}$. (b) Decay rates Γ_{ij} for the same combinations of $\boldsymbol{\wp}$ and $\boldsymbol{r}_{ij}$.

the single-atom Lamb shift is incorporated into ω_e since otherwise Eq. (2.11a) would diverge when $r_{ij} \to 0$. The exchange rates J_{ij} with $i \neq j$ originate form the exchange of the virtual transverse photons between atoms i and j [18]. In Fig. 2.1 we show the spatial dependence of the exchange and decay rates for different orientations of the atomic dipole moment.

The last step is to define an appropriate atomic operator $\hat{Q}$ and plug it into Eq. (2.8) to obtain the Master Equation for the density matrix. Since Q is an arbitrary combination of atomic operators, we can use

$$\hat{Q}(t) = \hat{\mathcal{P}}_{\beta,\alpha}(t) = e^{i\frac{\mathcal{H}}{\hbar}t} |\beta\rangle \langle\alpha| e^{-i\frac{\mathcal{H}}{\hbar}t}, \tag{2.12}$$

where $\hat{\mathcal{P}}_{\alpha,\beta}(t)$ can be referred as transition operator for the atomic states. We choose this operator because the matrix elements of the density operator for the atomic system satisfy the following relation [19]

$$\begin{aligned}\hat{\rho}^{(A)}_{\alpha,\beta}(t) &= \langle\alpha| \mathrm{Tr}_R\{\hat{\rho}(t)\} |\beta\rangle = \mathrm{Tr}_R\{\langle\alpha| \hat{\rho}(t) |\beta\rangle\} = \mathrm{Tr}_R\{\langle\alpha| e^{-i\frac{\mathcal{H}}{\hbar}t} \hat{\rho}(0) e^{i\frac{\mathcal{H}}{\hbar}t} |\beta\rangle\} \\ &= \mathrm{Tr}_R\{\hat{\rho}(0) e^{i\frac{\mathcal{H}}{\hbar}t} |\beta\rangle \langle\alpha| e^{-i\frac{\mathcal{H}}{\hbar}t}\} = \mathrm{Tr}_R\{\hat{\rho}(0) \hat{\mathcal{P}}_{\beta,\alpha}(t)\} \\ &= \langle\hat{\mathcal{P}}_{\beta,\alpha}(t)\rangle \ ,\end{aligned} \tag{2.13}$$

where $\hat{\rho}^{(A)}$ is the reduced density matrix of the atomic ensemble, $\hat{\rho}$ is the total density matrix of the system, and Tr_R denotes a trace over the degrees of freedom of the free-space radiation field (also known as *reservoir*). Since we care only about the reduced density matrix, from now on we shall omit the superscript and denote it as $\hat{\rho}$. We can write the master equation for the reduced density matrix by substituting Eq. (2.12) into Eq. (2.8) and specifying the total number of atoms. Thus, for every element of density matrix we have to calculate

$\dot{\hat{\rho}}_{\alpha,\beta}(t) = \langle \dot{\hat{\mathcal{P}}}_{\beta,\alpha}(t) \rangle$, or equivalently

$$\begin{aligned}\dot{\hat{\rho}}(t) = &\sum_{j}^{N} i\Delta \left[\hat{\sigma}_j^\dagger \hat{\sigma}_j, \hat{\rho}\right] + \sum_{j}^{N} i \left[\Omega_j e^{i(\boldsymbol{k}_c \cdot \boldsymbol{r}_j)} \hat{\sigma}_j^\dagger + \Omega_j^* e^{-i(\boldsymbol{k}_c \cdot \boldsymbol{r}_j)} \hat{\sigma}_j, \hat{\rho}\right] \\ &- \sum_{i \neq j} i J_{ij} \left[\hat{\sigma}_i^\dagger \hat{\sigma}_j, \hat{\rho}\right] + \sum_{i,j} \Gamma_{ij} \left[\hat{\sigma}_i \hat{\rho} \hat{\sigma}_j^\dagger - \frac{1}{2}\left(\hat{\sigma}_i^\dagger \hat{\sigma}_j \hat{\rho} + \hat{\rho} \hat{\sigma}_i^\dagger \hat{\sigma}_j\right)\right] .\end{aligned} \tag{2.14}$$

Equation (2.14) is the master equation of the ensemble of N atoms and it can also be written in the Lindbland form as

$$\dot{\hat{\rho}}(t) = -\frac{i}{\hbar}\left[\mathcal{H}_S, \hat{\rho}\right] + \mathcal{L}\left[\hat{\rho}\right] \tag{2.15}$$

where $\mathcal{H}_S$ is the Hermitian Hamiltonian of the system, while $\mathcal{L}\left[\hat{\rho}\right]$ describes the non-Hermitian dynamics of the system due to the coupling to a Markovian reservoir [13]. In our case these two terms are given by

$$\mathcal{H}_S = -\sum^{N} \hbar\Delta \hat{\sigma}_j^\dagger \hat{\sigma}_j - \sum_{j}^{N} \hbar \left(\Omega_j e^{i(\boldsymbol{k}_c \cdot \boldsymbol{r}_j)} \hat{\sigma}_j^\dagger + \text{H.c.}\right) + \sum_{i \neq j}^{N} \hbar J_{ij} \hat{\sigma}_i^\dagger \hat{\sigma}_j \,, \tag{2.16a}$$

$$\mathcal{L}\left[\hat{\rho}\right] = \sum_{i,j}^{N} \Gamma_{ij} \left[\hat{\sigma}_i \hat{\rho} \hat{\sigma}_j^\dagger - \frac{1}{2}\left(\hat{\sigma}_i^\dagger \hat{\sigma}_j \hat{\rho} + \hat{\rho} \hat{\sigma}_i^\dagger \hat{\sigma}_j\right)\right] . \tag{2.16b}$$

Note that for N non-interacting atoms there are 2^N atomic states and $N+1$ energy levels with the degeneracy of every energy level being

$$W(n_g) = \frac{N!}{n_g!(N-n_g)!} \,, \tag{2.17}$$

where n_g is the number of atoms in the ground state $|g\rangle$. On the other hand, a system with N interacting two-level atoms has 2^N states and in general non-degenerate energy levels.

Now that we have the master equation we can solve the differential equations for each density matrix element to see how the atomic populations and the coherences are distributed and evolve with time. However, there are only a few special cases that admit analytic solutions of these coupled equations, and thus the solutions must in general be obtained numerically.

2.1.1 Analytical solution for interacting pair of atoms

In this section, we present and discuss the case of two dipole-dipole interacting atoms, one of the very few cases that Eq. (2.14) accommodates analytical solution [20]. This is the first step in order to understand how the smallest system evolve in time and also reveal the super and subradiance with atoms. Although this system has analytical solution, we will also solve it numerically and verify the consistency of our results in Section 2.2.3.1. Other than the pair of atoms, there is an analytical solution for three atoms placed in an equilateral triangle configuration [21].

Consider a pair of atoms placed in distance r_{ij} as shown in Fig. 2.2(b). As discussed in Sec. 2.1, the atoms are coupled through the free radiation field which results in the cooperative frequency shift $J_{12} = J_{21}$ and cooperative decay rate $\Gamma_{12} = \Gamma_{21}$, both being functions of the interatomic distance and the direction of $\boldsymbol{\wp}$ with respect to $\boldsymbol{r}_{ij}$, see Eqs. (2.9). Before we

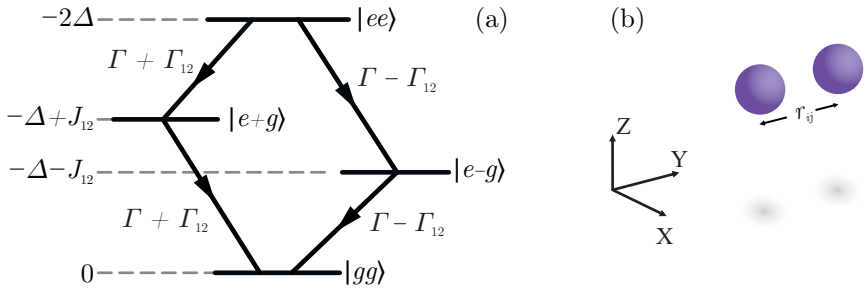

Figure 2.2: (a) Energy level diagram ($\hbar = 1$), in the rotating frame, for a coupled pair of atoms with the two possible decay channels. With the cooperative decay rate $\Gamma_{12} > 0$, the decay channels are distinguished as superradiant, with decay rate $\Gamma + \Gamma_{12}$, and subradiant with decay rate $\Gamma - \Gamma_{12}$. (b) Schematic of two atoms placed in distance r_{ij} and coupled through the free-space radiation field.

proceed to the solution of the density matrix we shall point out that there are two equivalent basis one can use, the bare or common basis and the diagonal basis

$$\begin{aligned} &\text{Bare basis} && \text{Diagonal basis} \\ &|ee\rangle = |e\rangle_1 |e\rangle_2 && |ee\rangle = |e\rangle_1 |e\rangle_2 \\ &|eg\rangle = |e\rangle_1 |g\rangle_2 && |e+g\rangle = (|eg\rangle + |ge\rangle)/\sqrt{2} \\ &|ge\rangle = |g\rangle_1 |e\rangle_2 && |e-g\rangle = (|eg\rangle - |ge\rangle)/\sqrt{2} \\ &|gg\rangle = |g\rangle_1 |g\rangle_2 && |gg\rangle = |g\rangle_1 |g\rangle_2 . \end{aligned} \tag{2.18}$$

Although it seems more simple to use the bare basis, it is convenient to choose the diagonal one because in this way we can get a better insight into frequency shifts, and super- and sub-radiant decay of the system.[1]

Now, we shall use Eq. (2.14) assuming that there is no external driving field ($\Omega = 0$) and write the corresponding differential equations in the diagonal basis

$$\dot{\rho}_{ee;ee} = -2\Gamma \rho_{ee;ee} \tag{2.19a}$$

$$\dot{\rho}_{e+g;e+g} = (\Gamma + \Gamma_{12})\, \rho_{ee;ee} - (\Gamma + \Gamma_{12})\, \rho_{e+g;e+g} \tag{2.19b}$$

$$\dot{\rho}_{e-g;e-g} = (\Gamma - \Gamma_{12})\, \rho_{ee;ee} - (\Gamma - \Gamma_{12})\, \rho_{e-g;e-g} \tag{2.19c}$$

$$\dot{\rho}_{gg;gg} = -\dot{\rho}_{ee;ee} - \dot{\rho}_{e+g;e+g} - \dot{\rho}_{e-g;e-g} \tag{2.19d}$$

$$\dot{\rho}_{ee;e+g} = i\,(\Delta + J_{12})\, \rho_{ee;e+g} - \frac{1}{2}\,(3\Gamma + \Gamma_{12})\, \rho_{ee;e+g} \tag{2.19e}$$

$$\dot{\rho}_{ee;e-g} = i\,(\Delta - J_{12})\, \rho_{ee;e-g} - \frac{1}{2}\,(3\Gamma - \Gamma_{12})\, \rho_{ee;e-g} \tag{2.19f}$$

$$\dot{\rho}_{ee;gg} = (i2\Delta - \Gamma)\, \rho_{ee;gg} \tag{2.19g}$$

$$\dot{\rho}_{e+g;e-g}(t) = -\,(i2J_{12} + \Gamma)\, \rho_{e+g;e-g} \tag{2.19h}$$

[1] In Sec. 2.2.3 we present a formal way to introduce the diagonal basis.

$$\dot{\rho}_{e+g;gg} = i\left(\Delta - J_{12}\right)\rho_{e+g;gg} + \left(\Gamma + \Gamma_{12}\right)\left(\rho_{ee;e+g} - \frac{1}{2}\rho_{e+g;gg}\right) \tag{2.19i}$$

$$\dot{\rho}_{e-g;gg}(t) = i\left(\Delta + J_{12}\right)\rho_{e-g;gg} - \left(\Gamma - \Gamma_{12}\right)\left(\rho_{ee;e-g} + \frac{1}{2}\rho_{e-g;gg}\right), \tag{2.19j}$$

where we used the notation $\rho_{u;v} = \langle u|\,\hat{\rho}\,|v\rangle$. Since the density matrix is by definition Hermitian operator, we wrote the equations for the upper triangular matrix.

The above set of equations could also be derived from the energy diagram given in Fig. 2.2 (a). These equations are easy to solve because they are almost decoupled and all of the same form. The first four equations obviously refer to diagonal matrix elements where we also used the density matrix property $\mathrm{Tr}\{\hat{\rho}\} = 1$. For sake of completeness we write the solutions of the diagonal elements which can reveal how the atomic populations evolve in time

$$\rho_{ee;ee} = \rho_{ee;ee}(0)e^{-2\Gamma t} \tag{2.20a}$$

$$\rho_{e+g;e+g} = e^{-\Gamma t}\left[\rho_{e+g;e+g}(0)e^{-\Gamma_{12}t} + \rho_{ee;ee}(0)\left(e^{-\Gamma_{12}t} - e^{-\Gamma t}\right)\frac{\Gamma + \Gamma_{12}}{\Gamma - \Gamma_{12}}\right] \tag{2.20b}$$

$$\rho_{e-g;e-g} = e^{-\Gamma t}\left[\rho_{e-g;e-g}(0)e^{\Gamma_{12}t} + \rho_{ee;ee}(0)\left(e^{\Gamma_{12}t} - e^{-\Gamma t}\right)\frac{\Gamma - \Gamma_{12}}{\Gamma + \Gamma_{12}}\right] \tag{2.20c}$$

$$\rho_{gg;gg} = 1 - \rho_{ee;ee} - \rho_{e+g;e+g} - \rho_{e-g;e-g}\,. \tag{2.20d}$$

As the interatomic distance decreases, $r_{12} \to 0$, cooperative decay rate approaches its maximum value, $\Gamma_{12} \to \Gamma$, and Eqs. (2.20b-c) reduce to

$$\rho_{e+g;e+g} \longrightarrow e^{-2\Gamma t}\left(\rho_{e+g:e+g}(0) + 2\Gamma t\rho_{ee;ee}(0)\right) \tag{2.21a}$$

$$\rho_{e-g;e-g} \longrightarrow \rho_{e-g;e-g}(0)\,, \tag{2.21b}$$

independent on the dipole moment polarization and the frequency shift. These equations reveal clearly two cases: (i) a fully excited pair of atoms decays to ground state solely through the symmetric path and emits photons with rate 2Γ, (ii) atoms in antisymmetric state, with almost zero interatomic distance, are unable to emit photons and decay to ground state, and thus the population in state $|e-g\rangle$ remain trapped [1, 15, 20].

As an example we examine how the pair of atoms evolves in time when the atoms are placed along y-axis with relative distance $r_{12} = (1/4)\lambda$, dipole moment along z-axis $\boldsymbol{\wp} = \wp\hat{z}$ (see Fig. 2.2(b)) and initial conditions $\rho_{ee;ee}(0) = 1\,, \rho_{e+g;e+g}(0) = \rho_{e-g;e-g}(0) = \rho_{gg;gg}(0) = 0$. These initial conditions correspond to a fully excited system with both atoms in the excited state. Figure 2.3(a) shows the evolution of population of every state and reveals that atomic system prefers a specific way to decay to ground state, as predicted by Dicke [1]. For the chosen configuration, the double excited state $|ee\rangle$ prefers to decay to ground state $|gg\rangle$ through the symmetric state $|e+g\rangle$. Obviously, the superradiant and subradiant channels are functions of the whole configuration, interatomic distance r_{12}, direction of atoms $\hat{\boldsymbol{r}}_{12}$, and dipole moment $\boldsymbol{\wp}$. Figure 2.3(b) corresponds to the same configuration with the only difference that atoms and dipole moment are both along z-axis. The results are similar but not exactly the same because of the different complex dipole-dipole exchange interaction,

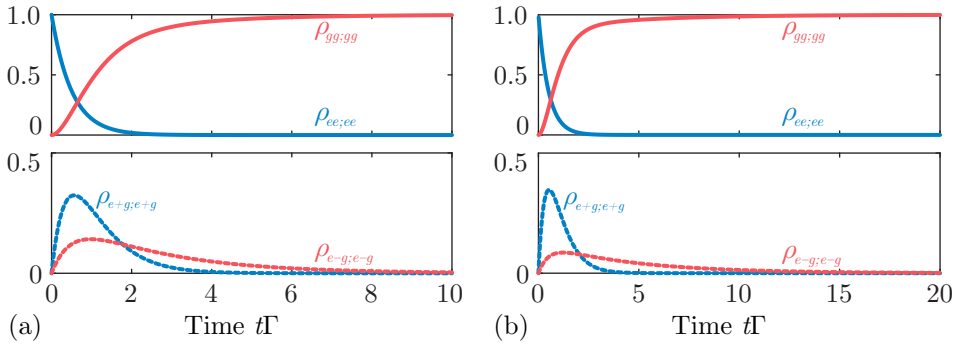

Figure 2.3: Time evolution of diagonal elements of density matrix for a pair of atoms with relative distance $r_{12} = \lambda/4$, dipole moment along z-axis, $\boldsymbol{\wp} = \wp\hat{z}$, and initial conditions $\hat{\rho}_{ee;ee}(0) = 1$. Graphs in column (a) depicts the case where atoms are placed along x-axis ($\boldsymbol{\wp} \perp \boldsymbol{r}_{12}$) and graphs in column (b) depicts the case where atoms are along z-axis ($\boldsymbol{\wp} \parallel \boldsymbol{r}_{12}$). In the first row we plot the double excited state population and the ground state population, while in the second the single excited symmetric and antisymmetric state population.

$\Gamma_{12}^{\parallel}(1/2) > \Gamma_{12}^{\perp}(1/2)$ as it is shown in Fig. 2.1(b). Due to the larger cooperative decay rate of parallel configuration, the symmetric state gains faster and more population but also decays faster to the ground state compared to the perpendicular configuration. Notice also that in the parallel case we let the system evolve for longer times because the subradiant channel has lower population and lower decay rate, as compared to the y-axis configuration, and thus needs more time to decay completely to ground state.

Hence, as the atoms are placed closed to each other, they decay stronger via the symmetric state channel. In the limit of all the atoms placed at the same point of the space, or extremely close $r_{ij} \lll \lambda_e$, the system decays to the ground state only through the symmetric states [1]. In the case of two atoms we can calculate analytically the probability of the system to decay through each path, the symmetric and the anti-symmetric. We can perform this calculation because these states do not interact or exchange population, something that happens for larger number of atoms $N > 2$. These two probabilities are given

$$P_+ = \frac{\Gamma + \Gamma_{12}}{2\Gamma} \tag{2.22a}$$

$$P_- = \frac{\Gamma - \Gamma_{12}}{2\Gamma}\,. \tag{2.22b}$$

In the limit of zero distance between the atoms the symmetric path probability approaches unity $P_+ \to 1$, while decoupled atoms, $r_{12} \gg \lambda_e$, would decay independently, $\Gamma_{12} = 0$ and $P_+ = P_- = 1/2$.

2.2 Quantum Stochastic Wavefunction Monte-Carlo

In this section we begin with the general formulation of the Quantum Stochastic Wavefunction method [13, 22]. Next we present a simple example of its functionality. Afterwards we apply this method to our system and reproduce the results of Fig. 2.3 using Monte-Carlo technique.

The time evolution of the reduced density matrix $\hat{\rho}$ of a quantum system is governed by

the master equation given in Eq. (2.15). We write it here again for sake of completeness,

$$\dot{\hat{\rho}}(t) = -\frac{i}{\hbar}\left[\mathcal{H}_S, \hat{\rho}\right] + \mathcal{L}\left[\hat{\rho}\right] , \tag{2.15}$$

where $\mathcal{H}_S$ the Hermitian Hamiltonian of the system and $\mathcal{L}[\hat{\rho}]$ describes the non-Hermitian dynamics of the system due to the coupling to a Markovian reservoir [13, 23]. In general, the Liouvillian $\mathcal{L}[\hat{\rho}]$ has the so-called Lindbland form

$$\mathcal{L}\left[\hat{\rho}\right] = \sum_j \Gamma_j \left[\hat{\sigma}_j \hat{\rho} \hat{\sigma}_j^\dagger - \frac{1}{2}\left(\hat{\sigma}_j^\dagger \hat{\sigma}_j \hat{\rho} + \hat{\rho}\hat{\sigma}_j^\dagger \hat{\sigma}_j\right)\right] , \tag{2.23}$$

where Γ_j is the decay or relaxation rate for channel j, and $\hat{\sigma}_j, \hat{\sigma}_j^\dagger$ are the corresponding lowering and raising operators of the system. It is convenient to separate the projective terms of Eq. (2.23) and re-write the master equation in different, but still equivalent form. Thus we define a non-Hermitian effective Hamiltonian of the system as

$$\mathcal{H}_{\text{eff}} \equiv \mathcal{H}_{\text{S}} - i\hbar \sum_j \frac{1}{2}\Gamma_j \hat{\sigma}_j^\dagger \hat{\sigma}_j \, , \tag{2.24}$$

and the so-called jump superoperator $\mathcal{L}_{\text{jump}}[\hat{\rho}] \equiv \sum_j \Gamma_j \hat{\sigma}_j \hat{\rho} \hat{\sigma}_j^\dagger$. The master equation (2.15) can be written as

$$\dot{\hat{\rho}} = -\frac{i}{\hbar}\left(\mathcal{H}_{\text{eff}}\hat{\rho} - \hat{\rho}\mathcal{H}_{\text{eff}}^\dagger\right) + \mathcal{L}_{\text{jump}}\left[\hat{\rho}\right] . \tag{2.25}$$

This equation reveals that the time-evolution of the density operator has two components, the first one is due to the effective Hamiltonian $\mathcal{H}_{\text{eff}}$, which is deterministic and continuous (although is non-Hermitian), and the second component is due to $\mathcal{L}_{\text{jump}}[\hat{\rho}]$ which yields discontinuous projections $\hat{\sigma}_j \hat{\rho} \hat{\sigma}_j^\dagger$, called quantum jumps, that preserves the trace of $\hat{\rho}$ throughout its evolution governed by the non-Hermitian $\mathcal{H}_{\text{eff}}$. Recall that density matrix can be written as a statistical mixture

$$\hat{\rho} = \sum_\Psi P_\Psi \left|\Psi\right\rangle \left\langle\Psi\right| , \tag{2.26}$$

where $|\Psi\rangle$ are pure states of the system. Hence, Eq. (2.25) can be written as

$$\frac{\partial \left|\Psi\right\rangle}{\partial \text{t}} \left\langle\Psi\right| + \left|\Psi\right\rangle \frac{\partial \left\langle\Psi\right|}{\partial \text{t}} = -\frac{i}{\hbar}\left(\mathcal{H}_{\text{eff}} \left|\Psi\right\rangle \left\langle\Psi\right| - \left|\Psi\right\rangle \left\langle\Psi\right| \mathcal{H}_{\text{eff}}^\dagger\right) + \sum_j \Gamma_j \hat{\sigma}_j \left|\Psi\right\rangle \left\langle\Psi\right| \hat{\sigma}_j^\dagger \, , \tag{2.27}$$

which suggests a very useful way of simulating the density operator of the system using the wavefunction approach and statistical averaging as described below.

Consider a wavefunction of the system $|\Psi\rangle$ evolving according to the Schrödinger equation

$$i\hbar \frac{\partial}{\partial \text{t}} \left|\Psi\right\rangle = \mathcal{H}_{\text{eff}} \left|\Psi\right\rangle . \tag{2.28}$$

We assume that at time $t = 0$ the state $|\Psi\rangle$ is normalized. Since $\mathcal{H}_{\text{eff}}$ is non-Hermitian, the norm of the wavefunction $|| \left|\Psi\right\rangle (t)|| \equiv \sqrt{\langle\Psi(t)|\Psi(t)\rangle}$ decreases with time. Physically, this is due to the fact that the system is not isolated but is interacting with the reservoir. The missing population of the decaying states of the system is thus leaking into the reservoir. For instance, imagine a two-level system coupled to free radiation filed: if a photon is emitted

into the reservoir at time t_1, it means that a jump occurred in one of the j possible decay channels which projects the wavefunction onto the corresponding state according to

$$|\Psi(t_1^+)\rangle = \frac{\hat{\sigma}_j |\Psi(t_1)\rangle}{\sqrt{\langle\Psi(t_1)| \hat{\sigma}_j^\dagger \hat{\sigma}_j |\Psi(t_1)\rangle}} \tag{2.29}$$

where t_1^+ denotes the instant time immediately after the quantum jump, while the denominator ensures the renormalization of the wavefunction. At any time $t \in [0, t_1]$, the probability density for the decay to occur into a particular channel j is given by

$$p_j(t) = \frac{||\sqrt{\Gamma_j}\hat{\sigma}_j |\Psi(t)\rangle||^2}{\sum_j ||\sqrt{\Gamma_j}\hat{\sigma}_j |\Psi(t)\rangle||^2} = \frac{\Gamma_j ||\hat{\sigma}_j |\Psi(t)\rangle||^2}{\sum_j \Gamma_j ||\hat{\sigma}_j |\Psi(t)\rangle||^2}\,, \tag{2.30}$$

where we used the notation $||\hat{\mathcal{A}}|\Psi\rangle|| = \sqrt{\langle\Psi|\hat{\mathcal{A}}^\dagger\hat{\mathcal{A}}|\Psi\rangle}$. The total probability $P(t)$ of the decay is a monotonous function of time (recall that we assumed Markovian reservoir) and it is given

$$P(t) = \sum_j \int_0^t \mathrm{d}t' p_j(t') = 1 - \langle\Psi(t)|\Psi(t)\rangle\ . \tag{2.31}$$

The above equation states that as the state $|\Psi\rangle$ evolves, under the action of the non-Hermitian $\mathcal{H}_{\text{eff}}$, its norm decreases which means that the system has increasing probability to decay through a quantum jump. In other words, an excited two-level system has zero probability of decaying at time $t = 0$ because $\langle\Psi(t)|\Psi(t)\rangle = 1$, however at times $t' > 0$ there is finite probability of the two-level system to decay to ground state because $\langle\Psi(t')|\Psi(t')\rangle < 1$.

Now we shall explain the algorithm to simulate this process. We take the normalised wavefunction $|\Psi(0)\rangle$ and propagate it with the Schrödinger equation using the effective Hamiltonian $\mathcal{H}_{\text{eff}}$, as in Eq. (2.28). This propagation continues until a jump occurs at time t_1. At this time t_1 the total probability satisfies the relation $P(t) = r_1$, where r_1 is a random number generated from a uniform distribution, $r_1 \in [0, 1]$. This number r_1 determined the total probability of a quantum jump, so if there are more than one decay channel we have to generate another random number q_1 and decide in which decay channel the jump occurred. We then continue the time-evolution by repeating the above steps. The next jump will be realised at a time t_2 where $P(t_2) = r_2$, the random number q_2 will point out the specific channel of the jump and accordingly project the wavefunction through Eq. (2.29). The whole process continues until we reach the desired final time t_{end} which, is usually large compared to the characteristic decay time of the system. This simulates a single quantum trajectory with the normalised wavefunction of the system $|\tilde{\Psi}(t)\rangle$ at any time $t \in [0, t_{\text{end}}]$ given by

$$|\tilde{\Psi}(t)\rangle = \frac{|\Psi(t)\rangle}{||\,|\Psi(t)\rangle\,||}\,. \tag{2.32}$$

The density operator corresponds to the ensemble-averaged state of a system. To obtain it, we can repeat the above process many times simulating $M \gg 1$ independent quantum trajectories and record the respective wavefunctions $|\tilde{\Psi}_m(t)\rangle$, where $m = 1, 2, 3, ..., M$. Then, we can asymptotically approach the density operator of the system as

$$\hat{\rho}(t) \simeq \frac{1}{M}\sum_m^M |\tilde{\Psi}_m(t)\rangle\langle\tilde{\Psi}_m(t)|\ . \tag{2.33}$$

Obviously, the larger the number of the simulated realizations M the better the approximation of Eq. (2.33). Now that we have a very close approximation of the density matrix we can calculate the expectation value for any system operator through

$$\langle \hat{\mathcal{A}}(t) \rangle = \mathrm{Tr}\left[\hat{\rho}(t)\hat{\mathcal{A}}\right] \simeq \frac{1}{M}\sum_{m}^{M} \langle \tilde{\Psi}_m(t)| \, \hat{\mathcal{A}}(t) \, |\tilde{\Psi}_m(t)\rangle \ . \tag{2.34}$$

An important feature of the Q.S.W. Monte-Carlo technique is that using this method one has only to deal with a wavefunction of dimension N, as opposed to working with the density matrix and its N^2 differential equations [23,24]. Hence, wavefunction simulations can provide solutions for systems with large Hilbert space where a direct solution of the density matrix is difficult due to limited computational memory [13, 23]. Moverover, since every trajectory is by default independent, these simulations can be distributed in different processors and be performed in parallel, resulting in a significant gain in computational power.

2.2.1 Spontaneous decay of a two-level atom

We first illustrate the method with a simplest example of spontaneous decay of an excited two-level system coupled to a reservoir via the Liouvillian [13, 25]

$$\mathcal{L}\left[\hat{\rho}\right] = \Gamma\left[\hat{\sigma}\hat{\rho}\hat{\sigma}^{\dagger} - \frac{1}{2}\left(\hat{\sigma}^{\dagger}\hat{\sigma}\hat{\rho} + \hat{\rho}\hat{\sigma}^{\dagger}\hat{\sigma}\right)\right] . \tag{2.35}$$

where for simplicity we assumed only a single decay channel. The effective non-Hermitian Hamiltonian and the stochastic jump operator are then

$$\mathcal{H}_{\text{eff}} = -\, i\hbar\frac{1}{2}\Gamma\hat{\sigma}^{\dagger}\hat{\sigma}\,, \tag{2.36a}$$

$$\mathcal{L}\left[\hat{\rho}\right] = \Gamma\hat{\sigma}\hat{\rho}\hat{\sigma}^{\dagger}\,. \tag{2.36b}$$

The Monte-Carlo simulations are realized via the following steps: (i) set the initial condition $|\Psi(0)\rangle = |e\rangle$, (ii) generate a random number $r \in [0,1]$, (iii) propagate the atomic wavefunction $|\Psi(t)\rangle = c_e(t)\,|e\rangle + c_g(t)\,|g\rangle$ with the Schroödinger equation using the effective Hamiltonian $\mathcal{H}_{\text{eff}}$ that yields the amplitude equations

$$\dot{c}_g = 0\,, \tag{2.37a}$$

$$\dot{c}_e = -\frac{1}{2}\Gamma c_e\,, \tag{2.37b}$$

(iv) the propagation is interrupted by the quantum jump at time t_1, which is determined by the condition

$$P(t_1) = 1 - \langle\Psi(t_1)|\Psi(t_1)\rangle = 1 - \left(|c_g(t_1)|^2 + |c_e(t_1)|^2\right) = r_1. \tag{2.38}$$

The wavefunction is then projected onto the ground state according to

$$|\Psi(t_1^+)\rangle = \frac{\hat{\sigma}\,|\Psi(t_1)\rangle}{\sqrt{\langle\Psi(t_1)|\,\hat{\sigma}^{\dagger}\hat{\sigma}\,|\Psi(t_1)\rangle}} = \frac{c_e(t_1)\,|g\rangle}{|c_e(t_1)|} \equiv c_g(t_1^+)\,|g\rangle\ , \tag{2.39}$$

where the global phase of wavefunction $|\Psi(t_1^+)\rangle$ that can be set zero without loss of generality [13]. In our example, the state vector will be projected onto ground at time $t \geq t_1$ and

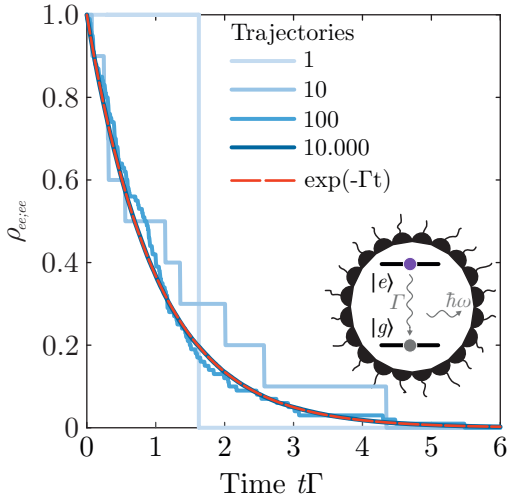

Figure 2.4: Monte-Carlo simulations of the ensemble averaged population of the excited state of a two-level atom coupled to a radiation reservoir, as obtained from different number of independent trajectories and compared to the analytical result (red dashed line). Inset: configuration of the Gedanken experiment in which the emitted by the atom photon is collected by ideally perfect photodetectors whose click signify a quantum jump of the atom to ground state.

remain there. This corresponds to a single trajectory, or numerical "experiment", and if we are interested in obtaining the density matrix we have to conduct many such experiments as per Eq. (2.33). Figure 2.4 shows the excited state population $\rho_{e;e}$ for different number of realizations. Obviously, as the number of realizations grows Eq. (2.33) approaches the analytic result $\rho_{e;e}(t) = e^{-\Gamma t}$, while in the case of just one quantum trajectory we can see how a two-level system abruptly decays to ground state via a quantum jump.

2.2.2 Driven two-level atom

Let us now expand the previous example and apply Monte-Carlo formalism to a driven two-level system coupled to reservoir. In the frame rotating with the frequency ω of the driving field, the Hamiltonian of the system is

$$\mathcal{H}_S = -\hbar\left(\Delta\hat{\sigma}^\dagger\hat{\sigma} + \Omega\hat{\sigma}^\dagger + \Omega^*\hat{\sigma}\right), \tag{2.40}$$

where we recall that $\Delta = \omega - \omega_{eg}$ is the detuning and $\Omega = \boldsymbol{\wp}\cdot\hat{\mathbf{e}}\mathcal{E}/\hbar$ is the Rabi frequency. For simplicity, we consider only one decay channel due to the spontaneous emission from the excited atomic state $|e\rangle$ and the Liouvillian is given by Eq. (2.35). Hence, the effective non-Hermitian Hamiltonian and the the jump superoperator are given

$$\mathcal{H}_{\text{eff}} = -\hbar\left[\left(\Delta + i\frac{1}{2}\Gamma\right)\hat{\sigma}^\dagger\hat{\sigma} + \Omega\hat{\sigma}^\dagger + \Omega^*\hat{\sigma}\right], \tag{2.41a}$$

$$\mathcal{L}\left[\hat{\rho}\right] = \Gamma\hat{\sigma}\hat{\rho}\hat{\sigma}^\dagger. \tag{2.41b}$$

We apply the Monte-Carlo method via the following steps: (i) set the initial conditions $|\Psi(t)\rangle = |g\rangle$, (ii) draw the first random number $r_1 \in [0,1]$, (iii) propagate the atomic wavefunction $|\Psi(t)\rangle = c_e(t)\,|e\rangle + c_g(t)\,|g\rangle$ with the Schrödinger equation using the effective Hamiltonian $\mathcal{H}_{\text{eff}}$, which yields the amplitude equations

$$\dot{c}_g = i\Omega^* c_e\,, \tag{2.42a}$$

$$\dot{c}_e = \left(i\Delta - \frac{1}{2}\Gamma\right)c_e + i\Omega c_g\,, \tag{2.42b}$$

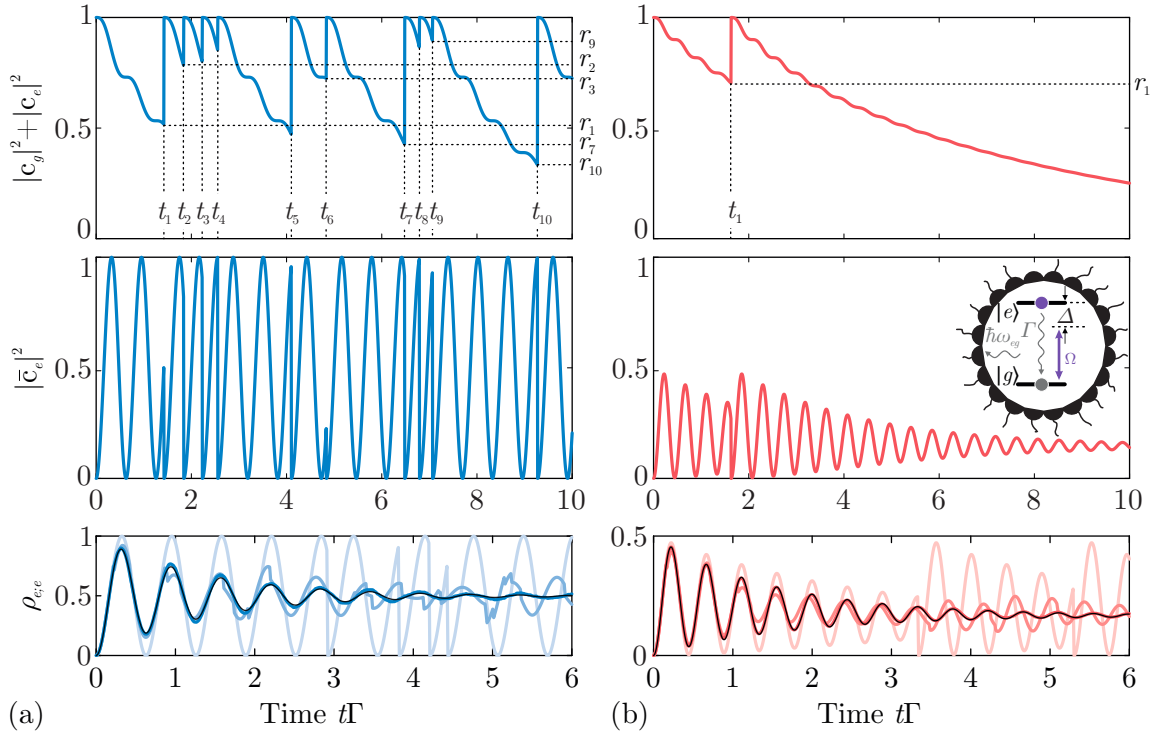

Figure 2.5: Monte-Carlo simulations for the dynamics of a two-level system driven by a classical field with $|\Omega| = 5\Gamma$ and detunings (a) $\Delta = 0$ and (b) $\Delta = 2|\Omega|$. Upper row: time evolution of the square of wavefunction norm $\langle\Psi(t)|\Psi(t)\rangle$ which is related to the decay probability as $P(t) = 1-\langle\Psi(t)|\Psi(t)\rangle$. Middle row: normalized population of the excited state $|\langle e|\Psi(t)\rangle|^2 = |\bar{c}_e|^2$. Lower row: Monte-Carlo simulations of the ensemble averaged population of the excited state $\rho_{e;e}$ obtained from different number (1, 10 and 1000) of realizations of independent realizations. The thin black lines correspond to the exact solutions of the density matrix equations [13, 25]. Inset: configuration of the Gedanken experiment.

(iv) the propagation is interrupted by the quantum jump at time t_1, which is determined by the condition

$$P(t_1) = 1 - \langle\Psi(t_1)|\Psi(t_1)\rangle = 1 - \left(|c_g(t_1)|^2 + |c_e(t_1)|^2\right) = r_1. \tag{2.43}$$

The wavefunction is then projected onto the ground state according to

$$|\Psi(t_1^+)\rangle = \frac{\hat{\sigma}\,|\Psi(t_1)\rangle}{\sqrt{\langle\Psi(t_1)|\,\hat{\sigma}^\dagger\hat{\sigma}\,|\Psi(t)\rangle}} = \frac{c_e(t_1)\,|g\rangle}{|c_e(t_1)|} \equiv c_g(t_1^+)\,|g\rangle\ . \tag{2.44}$$

We then continue the simulation by using $|\Psi(t_1^+)\rangle$ as the initial condition for step (ii) and follow the same procedure to determine the second quantum jump at time $t = t_2$, and so forth till reaching the desired final time $t_{\rm end}$.

In Fig. 2.5 we show single quantum trajectories for a two-level system driven by a classical laser with Rabi frequency $|\Omega| = 5\Gamma$ and two different detunings Δ. The upper plots reveal the time evolution of the square of the norm of the wavefunction $|\Psi(t)\rangle$, $\langle\Psi(t)|\Psi(t)\rangle = |c_g(t)|^2 + |c_e(t)|^2$, along with the random numbers $r_1, r_2, r_3, ...$ and the corresponding jump

times $t_1, t_2, t_3, \ldots$. The middle plots of Fig. 2.5 show the normalized population of the excited state,

$$|\langle e|\Psi(t)\rangle|^2 \equiv |\bar{c}_e(t)|^2 = \frac{|c_e(t)|^2}{|c_g(t)|^2 + |c_e(t)|^2} .$$

Although we use the same Rabi frequency Ω in both cases shown in Fig. 2.5, the presence of detuning, $\Delta \neq 0$, decreases the population of the excited state $|e\rangle$ and therefore slows the buildup of the decay probability $P(t) = \int \mathrm{d}t' \Gamma |c_e(t')|^2$ between the quantum jumps. Due to finite detuning $\Delta \neq 0$ the atom feels an effective Rabi frequency $\Omega_{\text{eff}} = \sqrt{|\Omega|^2 + |\Delta/2|^2}$ exhibiting faster oscillation. In the third row of Fiq. 2.5 we plot the populations of the excited state $\rho_{e;e}$ and the exact solution obtained in [13, 25], which verifies that the Monte-Carlo technique can reproduce the density matrix with high accuracy when the number of independent trajectories is large enough (in this example $M = 1000$).

2.2.3 Ensemble of interacting atoms

We can apply the QSW Monte-Carlo method to simulate the dynamics of N interacting two-level atoms, see Eqs. (2.15), (2.16). The Hamiltonian of the system and the Linbland operator $\mathcal{L}[\hat{\rho}]$ are

$$\mathcal{H}_S = \sum_{i \neq j}^{N} \hbar J_{ij} \hat{\sigma}_i^\dagger \hat{\sigma}_j \tag{2.45}$$

$$\mathcal{L}[\hat{\rho}] = \sum_{i,j}^{N} \Gamma_{ij} \left[\hat{\sigma}_i \hat{\rho} \hat{\sigma}_j^\dagger - \frac{1}{2} \left(\hat{\sigma}_i^\dagger \hat{\sigma}_j \hat{\rho} + \hat{\rho} \hat{\sigma}_i^\dagger \hat{\sigma}_j \right) \right] . \tag{2.46}$$

For simplicity we did not include a driving field which can be easily added via extra terms in the Hamiltonian. It is obvious that Eq. (2.46) is slightly different from the cases discussed above and we cannot directly apply the Monte-Carlo technique. The projective operator, first term in Eq. (2.46), acts on to two different atoms due to the collective decay character of the system. But we can cast Eq. (2.46) in the standard form of Eq. (2.23) by diagonalizing the Hermitian matrix Γ_{ij} by a unitary transformation V_{mi} [23],

$$\Gamma_{ij} = \sum_{n=1}^{N} V_{in} \gamma_n \left(V_{nj}\right)^\dagger \qquad (i, j = 1, ..., N) , \tag{2.47}$$

with eigenvalues $\gamma_n \geq 0$, and defining the collective jump operators

$$\hat{S}_n = \sum_{j=1}^{N} \hat{\sigma}_j V_{jn} , \tag{2.48}$$

which consist of a linear combination of single atomic operators $\hat{\sigma}$. We substitute the last two equations into Eq. (2.46) to obtain

$$\begin{aligned} \mathcal{L}[\hat{\rho}] &= \sum_{n}^{N} \gamma_n \left[\hat{S}_n \hat{\rho} \hat{S}_n^\dagger - \frac{1}{2} \left(\hat{S}_n^\dagger \hat{S}_n \hat{\rho} + \hat{\rho} \hat{S}_n^\dagger \hat{S}_n \right) \right] \\ &\equiv \sum_{n}^{N} \gamma_n \hat{S}_n \hat{\rho} \hat{S}_n^\dagger - \sum_{i,j}^{N} \Gamma_{ij} \frac{1}{2} \left(\hat{\sigma}_i^\dagger \hat{\sigma}_j \hat{\rho} + \hat{\rho} \hat{\sigma}_i^\dagger \hat{\sigma}_j \right) . \end{aligned} \tag{2.49}$$

We can now write the effective Hamiltonian and the jump superoperator as

$$\mathcal{H}_{\text{eff}} = \sum_{i\neq j}^{N} \hbar J_{ij} \hat{\sigma}_i^\dagger \hat{\sigma}_j - i \sum_{i,j}^{N} \hbar \frac{1}{2} \Gamma_{ij} \hat{\sigma}_i^\dagger \hat{\sigma}_j \,, \tag{2.50a}$$

$$\mathcal{L}_{\text{jump}}\left[\hat{\rho}\right] = \sum_{n}^{N} \gamma_n \hat{S}_n \hat{\rho} \hat{S}_n^\dagger \,. \tag{2.50b}$$

The superoperator written in the collective form shows that every quantum jump affects, in general, all the atoms and thus every atom has a probability of decaying depending both on the collective decay rates γ_n and the operators $\hat{S}_n$. In other words, a quantum jump projects the system to a superposition of states with one less excitation. It is evident that when the atoms are placed far from each other $r_{ij} \gg \lambda_e$ the interaction is vanishing, and the decay rates upon diagonalization become equal to single-atom spontaneous decay rates $\gamma_n \to \Gamma$ while the lowering operators reduce to $\hat{S} \to \hat{\sigma}$ with each channel n corresponding to n-th atom. On the other hand, if the atoms are placed extremely close to each other $r_{ij} \ll \lambda_e$, all the decay rates are zero $\gamma_n = 0$ except for the channel with the fully symmetric decay operator $\hat{S}_+ = \sum_j \hat{\sigma}_j / \sqrt{N}$ which has the maximum decay rate $\gamma_+ = N\Gamma$ [1]. This corresponds to superradiance as was first discussed by Dicke in 1954 [1] who showed that in a fully excited superradiant system, spontaneous emission takes place over a time scale inversely proportional to the number of radiated atoms as the system decays through symmetric states, and the highest decay rate $\propto N^2$ occurs when the system has $N/2$ excitations.

2.2.3.1 Numerical solutions for a pair of atoms

Consider now two interacting two-level atoms with interactomic distance r_{12}. We diagonalize the decay matrix Γ_{ij} and obtain the collective decay channels with eigenvalues

$$\gamma_1 = \Gamma + \Gamma_{12} \qquad \text{and} \qquad \gamma_2 = \Gamma - \Gamma_{12} \,, \tag{2.51}$$

and the corresponding the eigenvectors (collective jump operators)

$$\hat{S}_1 = \frac{1}{\sqrt{2}} \left(\hat{\sigma}_1 + \hat{\sigma}_2\right) \qquad \text{and} \qquad \hat{S}_2 = \frac{1}{\sqrt{2}} \left(\hat{\sigma}_1 - \hat{\sigma}_2\right) \,, \tag{2.52}$$

that are linear combinations of the atomic lowering operators. We apply the Monte-Carlo method via the following steps: (i) set the initial conditions $|\Psi(t)\rangle = |ee\rangle$, (ii) draw the first random number $r_1 \in [0, 1]$, (iii) propagate the atomic wavefunction

$$|\Psi(t)\rangle = c_{ee}(t)\,|ee\rangle + c_{e+g}(t)\,|e+g\rangle + c_{e-g}(t)\,|e-g\rangle + c_{gg}(t)\,|gg\rangle \tag{2.53}$$

[1] Obviously, there cannot be higher decay rates because, no matter the basis, according to linear algebra $\text{Tr}[\Gamma_{ij}] = \text{Tr}[\gamma_n] = N\Gamma$.

with the Schrödinger equation using the effective Hamiltonian $\mathcal{H}_{\text{eff}}$ for $N = 2$ given in Eq. (2.50a), which yields the amplitude equations

$$\dot{c}_{ee} = -\Gamma \tilde{c}_{ee} \tag{2.54a}$$

$$\dot{c}_{e+g} = \left[-iJ_{12} - \frac{1}{2}(\Gamma + \gamma_{12})\right] c_{e+g} \tag{2.54b}$$

$$\dot{c}_{e-g} = \left[iJ_{12} - \frac{1}{2}(\Gamma - \gamma_{12})\right] c_{e-g} \tag{2.54c}$$

$$\dot{c}_{gg} = 0\,. \tag{2.54d}$$

(iv) The propagation is interrupted by the quantum jump at time t_1, which is determined by the condition $P(t_1) = 1 - \langle\Psi(t_1)|\Psi(t_1)\rangle = r_1$. (v) Draw a random number $q \in [0,1]$ to decide in which channel the jump occurred: $q \in [0,p)$ corresponds to a jump in channel $n = 1$ and $q \in [p,1]$ corresponds to a jump in decay channel $n = 2$, with p given by

$$p = \frac{\gamma_1 ||\hat{S}_1 |\Psi(t_1)\rangle||^2}{\sum_{n=1,2} \gamma_n ||\hat{S}_n |\Psi(t_1)\rangle||^2}\,. \tag{2.55}$$

The wavefunction is then projected onto singly-excited state via channel n

$$|\Psi(t_1^+)\rangle = \frac{\hat{S}_n |\Psi(t_1^+)\rangle}{\sqrt{\langle\Psi(t_1^+)| \hat{S}_n^\dagger \hat{S}_n |\Psi(t_1^+)\rangle}} = c_{e\pm g}(t_1^+)\,|e \pm g\rangle\,. \tag{2.56}$$

We then continue the simulation by using $|\Psi(t_1^+)\rangle$ in step (ii) and follow the same procedure to determine the second quantum jump at time $t = t_2$ and reach the ground state $|gg\rangle$.

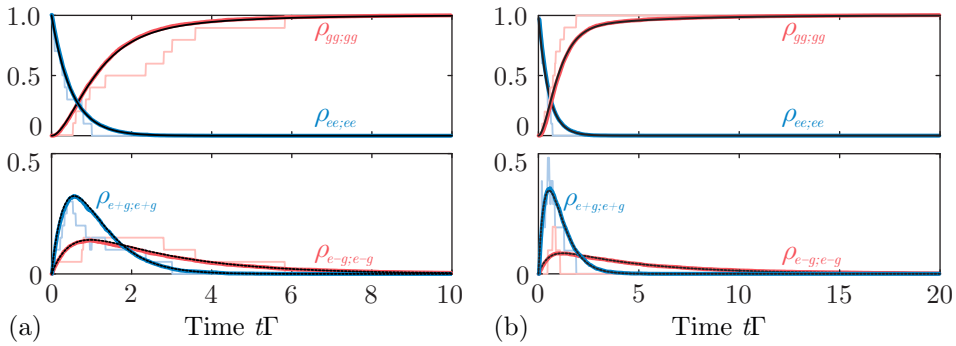

Figure 2.6: Monte-Carlo simulation of time evolution of a pair of interacting atoms with relative distance $r_{12} = \lambda_e/4$, dipole moment along the z-axis, $\boldsymbol{\wp} = \wp\hat{z}$, and initial conditions $\hat{\rho}_{ee;ee}(0) = 1$. Graphs in column (a) depicts the case with the atoms placed along x-axis ($\boldsymbol{\wp} \perp \boldsymbol{r}_{12}$) and graphs in column (b) are for atoms along the z-axis ($\boldsymbol{\wp} \parallel \boldsymbol{r}_{12}$). In the first row we plot the ensemble averaged population of the double excited state population and the ground state population, while in the second the population of the single excited symmetric and antisymmetric states obtained from $M = 10$ (light blue and light red lines) and $M = 1000$ (blue and red lines) independent realizations of the quantum trajectories. The thin black lines correspond to the exact solutions of the density matrix equations shown in Eq. 2.20.

It turns out that the collective lowering operators $\hat{S}_{1,2}$ define two distinct paths and as a result the double excited state can decay to the ground state by two sequential jumps via either symmetric channel or antisymmetric channel. This is a special case for two atoms and is due to the fact that the non-Hermitian effective Hamiltonian $\mathcal{H}_{\text{eff}}$[1] and the collective decay matrix Γ_{ij} have simultanously the same (right) eigenvectors, which does not hold true for $N \geq 3$. We will discuss this interesting feature in more detail in Chapter 4.

Figure 2.6 shows the results of Monte-Carlo simulations of the dynamics of two interacting atoms placed at a distance $r_{12} = \lambda_e/4$ and compares them with the exact solution of the density matrix derived in Sec. 2.1.1 (see Fig. 2.2). These results verify that for many ($M = 1000$) independent realizations of quantum trajectories the ensemble averaged results are indistinguishable from the exact ones obtained from the solution of the density matrix equations. In the case of $M = 10$ realizations we get an approximate solution for the density matrix.

[1]The solution of the eigenvalue problem $\mathcal{H}_{\text{eff}} |\Psi\rangle = \hbar\lambda_n |\Psi\rangle$ results in 2^N generally nonorthogonal right-eigenstates with complex eigenvalues λ_n. The real part of each eigenvalue $\mathfrak{Re}(\lambda_n) = \delta_n$ determines the level shift δ_n of the corresponding eigenstate from the single-atom resonance, while the imaginary part $\mathfrak{Im}(\lambda_n) = -\tilde{\gamma}_n$ yields the level width $\tilde{\gamma}_n$ of the eigenstate [4].

Chapter 3

Enhanced Optical Cross Section

The purpose of this chapter is to demonstrate the capabilities of spatially-periodic atomic ensembles to dramatically increase the strength of the light-matter interaction at the single-photon level. For a single atomic dipole in free-space the excitation probability does not exceed 10% [26] and is typically limited by the focusing strength of the lens [26]. However the excitation probability can be further enhanced using cavities or waveguides achieving the celebrated *strong coupling* regime associated with cavity QED [27, 28]. Here, we replace the single dipole with an ensemble of identical dipoles aiming to take advantage of the strong dipole-dipole interactions (multiple scattering) that leads to a collective response resulting in enhanced (superradiance) or reduced (subradiance) scattering rates [8]. In the first section, we present the single excitation approximation, underline its limitations and explain how these affect our approach to the problem. In the second section, we explore the collective behavior of atoms in perfect two-dimensional lattices and examine their capabilities in reflecting, focusing and deflecting an incoming single photon in a Gaussian mode.

3.1 Single excitation approximation

In this approximation we assume the atomic ensemble can contain only one excitation distributed in N atoms at a time. Physically this means that the system is driven by a weak laser field or a wavepacket that contains at most one photon. Multiple excitations of small atomic ensembles will be considered in Chapter 4. The single-excitation assumption allows us to truncate the exponentially large Hilbert space of dimension 2^N for N two-levels atoms to a much smaller subspace of dimension $N+1$ that allows us to consider many atoms $N \gg 1$.

3.1.1 Atoms

Consider $N \gg 1$ two-level atoms with the ground state $|g\rangle$ and the excited state $|e\rangle$ interacting with a weak (quantum) field $\boldsymbol{E}(\boldsymbol{r})$ on the dipole transition $|g\rangle \to |e\rangle$. The Hamiltonian of the system is [4]

$$\mathcal{H} = \sum_{\boldsymbol{k}} \hbar\omega_{\boldsymbol{k}} \hat{a}^\dagger_{\boldsymbol{k}} \hat{a}_{\boldsymbol{k}} + \sum_{j=1}^{N} \hbar\omega_e \hat{\sigma}^\dagger_j \hat{\sigma}_j - \sum_{j}^{N} \left[\wp \boldsymbol{\sigma} \cdot \boldsymbol{E}(\boldsymbol{r}_j) \hat{\sigma}^\dagger_j + \text{H.c.} \right] , \tag{3.1}$$

where we set the energy of the ground state to zero, $\hbar\omega_e = \hbar\omega_{eg}$, and made the RWA for atom-field coupling. We will take advantage of the results obtained through the derivation of

the master equation in Sec. 2.1 by eliminating the vacuum modes of the radiation field and making use of the effective Hamiltonian given in Eq. (2.16a).

Considering a single atomic excitation, the state vector can be expanded as

$$|\Psi\rangle = \sum_{j}^{N} b_j |e_j\rangle + C |G\rangle , \tag{3.2}$$

where $|G\rangle \equiv |g_1, g_2, g_3, ..., g_N\rangle$ is the collective ground state of the atoms, and $|e_j\rangle \equiv |g_1, g_2 , ..., e_j, ... , g_N\rangle$ denote the states with atom j excited and all the other atoms in the ground state. The state vector in Eq. (3.2) evolves in time according to the Schrödinger equation $\partial_t |\Psi\rangle = -(i/\hbar)\mathcal{H}_{\text{eff}} |\Psi\rangle$, leading to the atomic amplitude equations

$$\dot{C} = \sum_{j}^{N} i\Omega_j^* e^{-i\boldsymbol{k}\cdot\boldsymbol{r}_j} b_j , \tag{3.3a}$$

$$\dot{b}_j = \left(i\Delta - \frac{1}{2}\Gamma\right) b_j - \frac{1}{2}\sum_{i\neq j} F_{ij} b_i + i\Omega_j e^{i\boldsymbol{k}\cdot\boldsymbol{r}_j} C , \tag{3.3b}$$

where Ω_j is the Rabi frequency of an incoming photon in the selected $\boldsymbol{k}$th mode with frequency ω and detuned by $\Delta = \omega - \omega_e$ at the position $\boldsymbol{r}_j$ of jth atom, and $F_{ij} = \Gamma_{ij} + i2J_{ij}$ is the complex dipole-dipole exchange interaction between the atoms given in Eq. (2.9) and (2.11). Since we are interested in the weak driving regime, the atomic system remains mainly to its collective ground state and rarely decays from the excited state via quantum jumps, which allows us to solve the amplitude equations without applying the jump superoperator of Chapter 2. The amplitude equations then yield

$$\dot{C} \simeq 0 \Rightarrow C \simeq 1, \tag{3.4a}$$

$$\dot{b}_j = \left(i\Delta - \frac{1}{2}\Gamma\right) b_j - \frac{1}{2}\sum_{i\neq j} F_{ij} b_i + i\Omega_j e^{i\boldsymbol{k}\cdot\boldsymbol{r}_j} . \tag{3.4b}$$

In the steady state $\dot{b}_j = 0$ we have a linear system of equations for amplitudes b_j:

$$\left(i\Delta - \frac{1}{2}\Gamma\right) b_j - \frac{1}{2}\sum_{n\neq m} F_{ij} b_i = -i\Omega_j e^{i\boldsymbol{k}\cdot\boldsymbol{r}_j} . \tag{3.5a}$$

3.1.2 Incoming beam

The above theory is applicable to any weak incoming field, and we shall assume a Gaussian beam with wave vector $\boldsymbol{k}||\hat{\boldsymbol{z}}$. Other than their simplicity and connection with experimental applications, Gaussiam beams are very important for the construction of mirrors and lenses via atomic ensembles [8, 12] as discussed below.

A Gaussian mode with waist w_0 at $z = 0$ has the form

$$\frac{E_{\text{G}}(x, y, z)}{E_0} = \frac{w_0}{w(z)} e^{-\frac{x^2+y^2}{w^2(z)}} e^{i(kz - \text{atan}(z/z_R))} e^{-ik\frac{x^2+y^2}{2R(z)}} \tag{3.6}$$

where the first exponent represents the transverse amplitude, the second exponent contains for longitudinal and Gouy phase, and the last exponent contains the radial phase of the beam,

$z_R = \pi w_0^2/\lambda_0$ denotes the Rayleigh length, and

$$w^2(z) = w_0^2\left[1+\left(\frac{\lambda_0 z}{\pi w_0^2}\right)^2\right] = w_0^2\left[1+\left(\frac{z}{z_R}\right)^2\right], \tag{3.7a}$$

$$R(z) = z\left[1+\left(\frac{\pi w_0^2}{\lambda_0 z}\right)^2\right] = z\left[1+\left(\frac{z_R}{z}\right)^2\right], \tag{3.7b}$$

are the beam waist and radius of curvature of the phase front at different z. Note that the Gaussian beam in the far-field $z \gg z_R$ approaches a dipole field.

3.1.3 Radiated field

The field at position $\boldsymbol{r} = \boldsymbol{r}_j + \boldsymbol{R}_j$ radiated by a dipole $\wp\boldsymbol{\varrho}$ placed at $\boldsymbol{r}_j$ has the form [17]

$$\begin{aligned}\boldsymbol{E}_{\text{dip}}(\boldsymbol{r}) &= \frac{k_0^2}{\epsilon_0}\overline{\overline{\mathbf{G}}}(\boldsymbol{R}_j,\omega_0)\wp\boldsymbol{\varrho} \\ &= \frac{k_0^2}{\epsilon_0}\frac{e^{ik_0R_j}}{4\pi R_j}\left[\left(\hat{\boldsymbol{R}}_j\times\wp\boldsymbol{\varrho}\right)\times\hat{\boldsymbol{R}}_j + \left(\frac{1}{k_0^2R_j^2}-\frac{i}{k_0R_j}\right)\left(3\hat{\boldsymbol{R}}_j\left(\hat{\boldsymbol{R}}_j\cdot\wp\boldsymbol{\varrho}\right)-\wp\boldsymbol{\varrho}\right)\right],\end{aligned} \tag{3.8}$$

where the first term in brackets denotes the polarization $\hat{\mathbf{e}} = (\hat{\boldsymbol{R}}_j \times \wp\hat{\boldsymbol{\varrho}}) \times \hat{\boldsymbol{R}}_j$ of the field in the far-field zone with $\hat{\mathbf{e}} \perp \boldsymbol{k}_0$. The operator for the field produced by an atom is related to the atomic lowering operator as [10]

$$\hat{\boldsymbol{E}}_j(\boldsymbol{r}) = \frac{k_e^2}{\epsilon_0}\overline{\overline{\mathbf{G}}}(\boldsymbol{R}_j,\omega_e)\wp\boldsymbol{\varrho}\,\hat{\sigma}_j\,, \tag{3.9}$$

while the expectation value for the radiated field is given by

$$\boldsymbol{E}_j(\boldsymbol{r}) = \text{Tr}\left[\rho\hat{\boldsymbol{E}}_j(\boldsymbol{r})\right] = \frac{k_e^2}{\epsilon_0}\overline{\overline{\mathbf{G}}}(\boldsymbol{R}_j,\omega_0)\wp\boldsymbol{\varrho}\,\langle\hat{\sigma}_j\rangle\,. \tag{3.10}$$

Consequently, the total field emitted by an atomic ensemble is

$$\boldsymbol{E}(\boldsymbol{r}) = \sum_j \boldsymbol{E}_j(\boldsymbol{r}) = \frac{k_e^2}{\epsilon_0}\sum_j \overline{\overline{\mathbf{G}}}(\boldsymbol{R}_j,\omega_e)\wp\boldsymbol{\varrho}\,\langle\hat{\sigma}_j\rangle\,. \tag{3.11}$$

In single excitation regime, the expectation values of the atomic operators are $\langle\hat{\sigma}_j\rangle = b_jC^* \simeq b_j$, and therefore the far-field Eq. (3.11) is

$$\boldsymbol{E}(\boldsymbol{r}) = \hat{\mathbf{e}}\frac{\wp k_e^2}{4\pi\epsilon_0}\frac{e^{ik_er}}{r}\sum_j b_j e^{-i\boldsymbol{k}_e\boldsymbol{r}_j}\,, \tag{3.12}$$

where $\boldsymbol{k}_e \equiv k_e\hat{\boldsymbol{r}}$, and we used the far-field approximation $R_j = |\boldsymbol{r}-\boldsymbol{r}_j| \simeq r$ for the amplitude and $R_j = |\boldsymbol{r}-\boldsymbol{r}_j| \simeq r - (\boldsymbol{r}\cdot\boldsymbol{r}_j)/r$ for the phase.

3.2 Collective response of spatially-periodic atomic ensembles

The collective response of two-dimensional atomic arrays interacting with incoming weak laser field was first presented by Bettles *et al.* [8] through numerical results, while Shahmoon [9] derived analytical formulae shading more light to the phenomenon. In this section, we show that 2D atomic arrays with subwavelenth interatomic distance can exhibit great variation in transmission and reflection of the probe field depending on their geometry. We explore the collective behavior for various configurations (random, square and triangular lattices) and present their performance both for continuous and pulsed schemes.

3.2.1 Single dipole

We begin with a simple example of a two-level atom interacting with the incoming Gaussian beam propagation along axis $\boldsymbol{k}||\hat{\boldsymbol{z}}$. The atomic dipole is driven by the total electric field and in the weak driving regime is given by

$$\wp_j = \alpha(\omega)\boldsymbol{E}(\boldsymbol{r}_j)\,, \tag{3.13}$$

where $\alpha(\omega)$ is the atomic polarizability given in the linear and isotropic regime by[1] [8, 9, 16]

$$\alpha(\omega) = -\frac{6\pi\epsilon_0}{k_e^3}\frac{1}{2\Delta/\Gamma + i}\,, \tag{3.14}$$

which is applicable when $|\Delta| = |\omega - \omega_e| \ll \omega_e$. To examine the extinction of the incoming resonant Gaussian beam by the field of a single atom, we calculate the total far-field of Eqs. (3.6)(3.8) on z axis

$$\boldsymbol{E}_{\rm tot}(z) = \boldsymbol{E}_{\rm dip}(z) + \boldsymbol{E}_{\rm inc}(z) \simeq i\frac{3E_0 e^{ik_e z}}{2kz}\left[1 - {\rm sgn}(z)\frac{k_e^2 w_0^2}{3}\right]\hat{\mathbf{e}}\,, \tag{3.15}$$

where ${\rm sgn}(z)$ is the sign of z and $\hat{\mathbf{e}}$ is the field polarization. This equation reveals that these fields can cancel each other in the $+z$ direction, while interfering constructively in the $-z$ direction, provided the condition $w_0^2 \simeq 3/k_e^2 = (0.276\lambda_e)^2$ is satisfied.

In Fig. 3.1 we plot the real and the imaginary part of the total field in Eq. (3.15) for a Gaussian field with waist $w_0 = 0.276\lambda_e$ showing how the incoming and the scattered fields interfere constructively and destructively in the backward and forward direction, respectively. Note that in the backward direction only the imaginary parts are in phase creating thus a standing wave.

3.2.2 Many interacting dipoles

The case of many atoms N is more involved since now the local field experienced by each atom is the sum of the external probe field and the fields scattered by the other $N-1$ atoms, namely

$$\boldsymbol{E}(\boldsymbol{r}_j) = \boldsymbol{E}_{\rm inc}(\boldsymbol{r}_j) + \sum_{i\neq j}^{N}\boldsymbol{E}_i(\boldsymbol{r}_j)\,. \tag{3.16}$$

[1] Generally, polarizability is a tensor, but for simplicity is taken as scalar/isotropic and identical for all the atoms

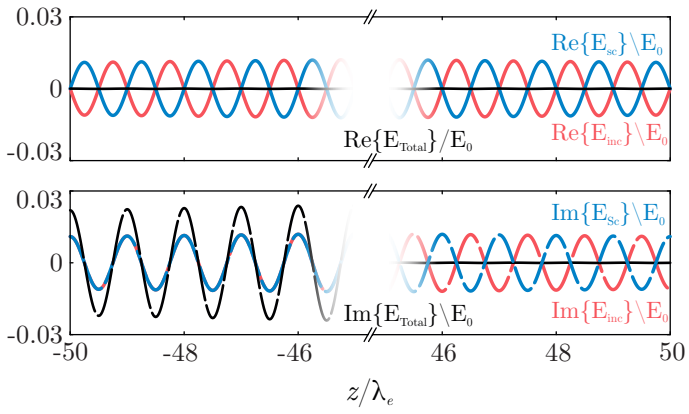

Figure 3.1: Numerical simulation of the total field emitted by a single atom driven by a Gaussian mode with $w_0 = 0.276\lambda_e$. Upper panel shows the real part of incoming (red), atomic (blue) and total field (black), while lower panel shows the respective imaginary parts on z-axis $(x, y = 0)$. Real parts interfere destructively in both directions while imaginary parts interfere constructively in the backward and destructively in the forward direction.

We substitute the above equation into Eq. (3.13) obtain the dipole moment for every atom

$$\wp_j = \alpha(\omega)\left[\boldsymbol{E}_{\rm inc}(\boldsymbol{r}_j) + \sum_{i\neq j}^{N} \boldsymbol{E}_i(\boldsymbol{r}_j)\right] = \alpha(\omega)\left[\boldsymbol{E}_{\rm inc}(\boldsymbol{r}_j) + \sum_{i\neq j}^{N} \frac{k_e^2}{\epsilon_0}\overline{\overline{\mathbf{G}}}(\boldsymbol{r}_{ji},\omega_e)\wp_i\right]. \tag{3.17}$$

The last equation can be solved numerically for modest N with arbitrary dipole positions and driving fields [29]. For atoms placed in infinite, defect-free lattices (square, triangular, hexagonal etc) one can also derive self-consistent analytic solutions [9]. We perform numerical studies aiming to examine finite and inhomogeneous atomic systems.

We can characterize the optical cross section by the percentage of the transmitted power, the smaller is the transmission the larger is the cross section. To measure the transmission, we calculate the total power passing through a finite surface (e.g. lens) on the right of it. The power is given by integrating the Poynting over a surface,

$$P = \frac{\epsilon_0 c^2}{2}\int_S \mathfrak{Re}\left[\boldsymbol{E}\times\boldsymbol{B}^*\right]\cdot \mathrm{d}\boldsymbol{S}\,, \tag{3.18}$$

where $\boldsymbol{B} = \boldsymbol{k}_e \times \boldsymbol{E}/c$ is the magnetic field and $\boldsymbol{E}$ is the electric field of a beam with wave vector $\boldsymbol{k}$, and $\mathrm{d}\boldsymbol{S} = \mathrm{d}S\hat{\boldsymbol{z}}$ is the surface differential area element. In our simulations we use a disk surface with radius $R = 100\lambda_e$, placed at $z = 150\lambda_e$ centered at $(x, y) = (0, 0)$. We define transmission $T = P/P_0$ as the ratio of the powers passing through the surface in the presence (P) and absence (P_0) of the dipoles. Alternatively, we can calculate the transmission, reflection and scattering by counting the rates of photons emitted in the incident Gaussian mode in the forward and backward direction as described in Appendix A and in ref. [30].

In the case of dilute atomic ensembles, every atom is driven only by the external field since dipole-dipole interaction falls off with distance as $1/(k_e r_{ij})$. Consequently, the total cross section is simply the sum of N independent two-level atoms and the transmission is governed by the density of the ensemble

$$T_{\rm ind} = e^{-\sigma_{\rm ind} D_{\rm 2D}} \tag{3.19}$$

where $\sigma_{\rm ind} = \sigma_0/[1+(2\Delta/\Gamma)^2]$ with $\sigma_0 = 3\lambda_e^2/(2\pi)$ being the resonant cross section of a single atom and $D_{\rm 2D}$ is the density of the two dimensional atomic cloud. This equation is similar to

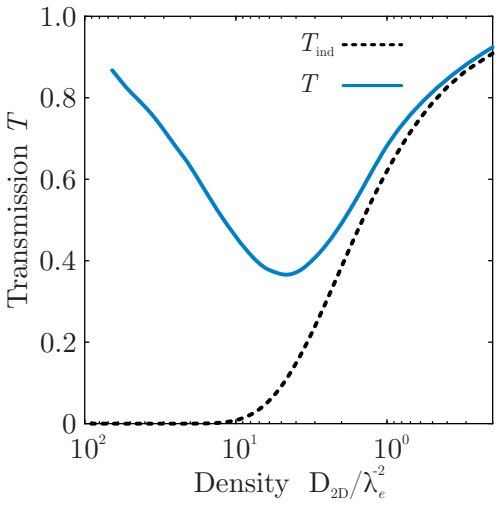

Figure 3.2: Transmission of a resonant ($\Delta = 0$) Gaussian mode through a random 2D cloud of $N = 150$ interacting atoms versus the density of the cloud. As the atomic density D_{2D} increases the transmission through the interacting monolayer (blue line) deviates from that for non-interacting dipoles (dotted line). Each data point is averaged over 200 realizations. Transmission $T = P/P_0$ is calculated using the power on a disk with radius $R = 100\lambda_e$, at $z = 150\lambda_e$ and centered at $(x, y) = (0, 0)$. We assumed a circularly polarized $\hat{\mathbf{e}} = (\hat{\boldsymbol{x}}+i\hat{\boldsymbol{y}})/\sqrt{2}$ beam with waist $w_0 = 2.5\lambda_e$ passing through the atomic layer at $z = 0$.

Beer–Lambert–Bouguer law relating the light attenuation to the properties of the material through which the light is traveling.

Figure 3.2 shows the transmission of a resonant ($\Delta = 0$) continuous–wave Gaussian beam passing through a two dimensional monolayer of uniformly randomly distributed interacting atoms (blue line). The same graph also includes the two dimensional limit of the celebrated Beer–Lambert–Bouguer law (black dotted line), Eq. (3.19), corresponding to the case of non-interacting atoms. This figure reveals that as the density of the ensemble is increased the transmission deviated significantly form the non-interacting value. This is due to the fact that dipole–dipole interactions introduce large frequency shifts and also affect the decay rate of collective states leading to a broadening and suppression of the overall absorption line shape, reducing the resonant extinction (increasing transmission) [8]. One may then mistakenly assume that placing interacting dipoles close to each other can only decrease the cross section, which is, however, not the case, as we explain below.

3.2.2.1 Ordered arrays of atoms

Bettles *et al.* [8] have shown that putting atoms in spatially ordered configuration, i.e. confining them in triangular or square lattices with small interatomic separations, can lead to transmission values much smaller than those obtained from random ensembles. The light attenuation and the collective cross-section exhibit resonant enhancement with the position of the resonance depending on the lattice constant. In Fig. 3.3 we present the power transmission of a resonant ($\Delta = 0$) continuous–wave Gaussian beam through the square and triangular arrays of atoms with various lattice constants. The graphs reveal the existence of *magic distances* between atoms that can behave as perfect mirrors for resonant light by achieving almost zero transmission and total reflection, with very little scattering. For square lattice we find that lattice constants $d = 0.2\lambda_e$ and $d = 0.79\lambda_e$ achieve the best performance ($T \sim 0$), while for triangular lattice we have $d = 0.21\lambda_e$ and $d = 0.87\lambda_e$. Although we refer to these lattice constants as *magic distances*, Shahmoon *et al.* [9] have presented analytical solutions and showed that for these distances collective resonances have zero frequency shift. Thus, the incoming resonant field couples and drives these states that produce the same field π out of phase. Another result is that the atomic arrays have interesting features mainly

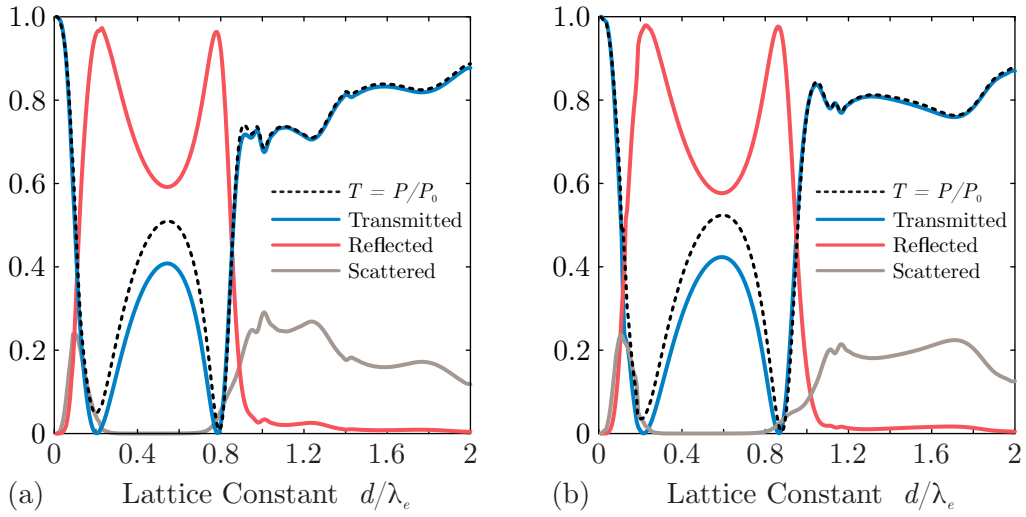

Figure 3.3: Resonant ($\Delta = 0$) optical power transmission and reflection of a Gaussian mode through (a) square and (b) triangular 2D arrays of $N = 25^2$ interacting atoms. Square lattice behaves like a perfect mirror for lattice constants $d = 0.2\lambda_e$ and $d = 0.79\lambda_e$, while triangular lattice reveal its best performance for $d = 0.21\lambda_e$ and $d = 0.87\lambda_e$. When the lattice constant is larger than the resonant wavelength $d > \lambda_e$ light is mainly transmitted and scattered but not reflected due to small dipole–dipole interaction and spontaneous emission. We also plot the transmission value $T = P/P_0$ (black dotted line) obtained using Eq. (3.18) proving that both methods are in very good agreement. We assumed a circularly polarized $\hat{\mathbf{e}} = (\hat{\boldsymbol{x}} + i\hat{\boldsymbol{y}})/\sqrt{2}$ beam with waist $w_0 = 2.5\lambda_e$ passing thought the atomic layer at $z = 0$.

for subwavelength lattice constants where the dipole–dipole interaction is strong enough to create distinct eigenstates with subradiant and superradiant decay rates. On the other hand, when the lattice constant is larger than the resonant wavelength $d > \lambda_e$ light is mainly transmitted and scattered but not reflected due to small dipole–dipole interaction and spontaneous emission in 4π solid angle. Another issue that has not yet been studied is the profile of the incoming field to match with corresponding atomic wavefunction: If these two wavefunctions do not fully overlap, the field will eventually interact with a superposition of collective atomic eigenstates.

In Fig. 3.4(a)-(c) we explore the collective eigenstates of the non-Hermitian Hamiltonian $\mathcal{H}_{\text{eff}}$ that have the largest overlap with the spatial profile of the incident field. Figure 3.4(a) shows the frequency shift of the most mode-matched atomic eigenstates in triangular lattice versus lattice constant and number of atoms, Fig 3.4(b) shows the line shape width of the same states, and Fig. 3.4(c) shows the overlap between the atomic eigenstate $|\Psi_{\text{Atom}}\rangle$ and profile of the incoming Gaussian field. Although Bettles *et al.* [8] stated that extinction cross section $(1 - T)$ scales inversely with linewidth and that subradiance results in an enhanced extinction, we find that superradiant states can achieve large extinction cross section if they overlap strongly with the incoming bosonic mode. In Fig. 3.4(d) we plot the transmission, reflection and scattering of a superradiant state with $\Gamma_{\text{Atom}} = 1.7\Gamma$. Hence, we are mainly interested in tuning the driving laser to eigenstates that have large overlap with the field profile. However, atoms placed in triangular lattice with period $d = 0.87\lambda_e$ create a perfect mirror and achieve extinction of $(1 - T) \simeq 0.01$ for resonant incoming light despite the poor overlap

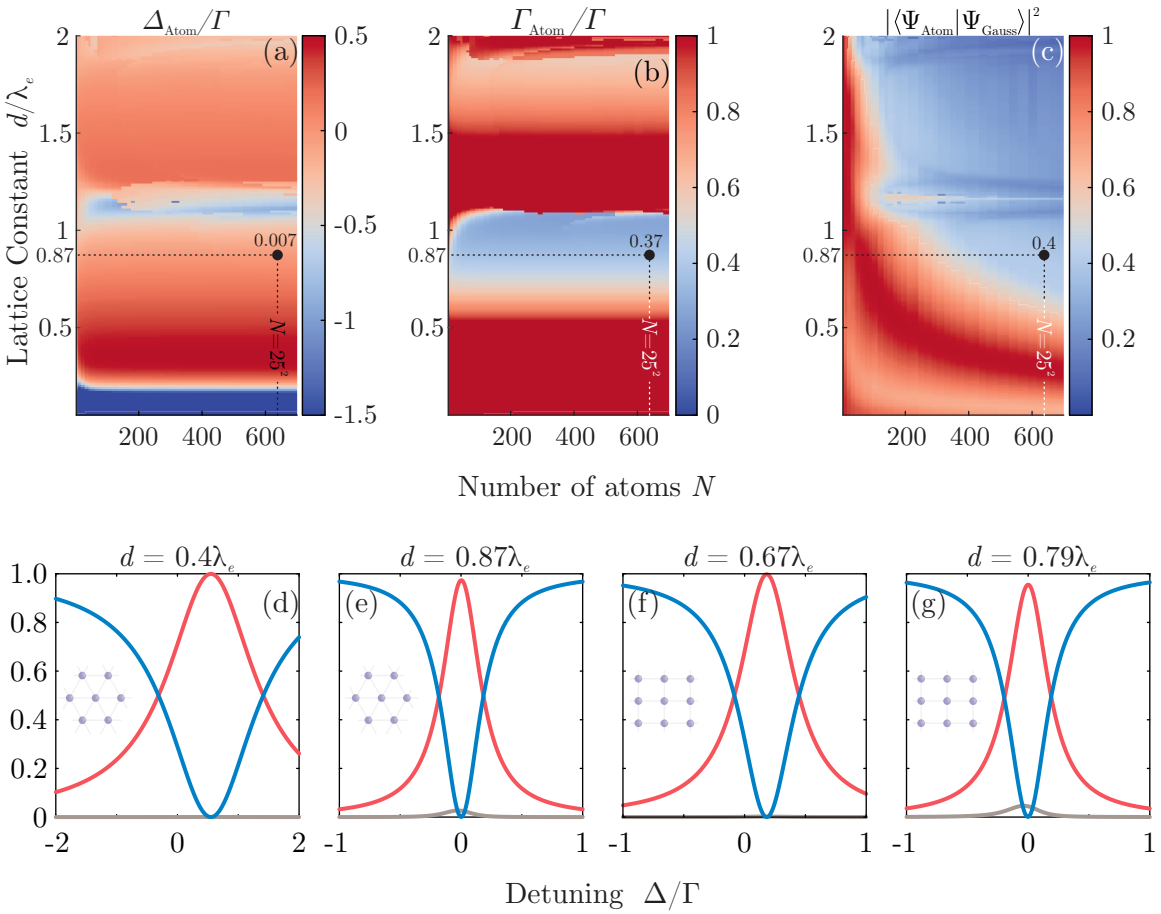

Figure 3.4: Characteristics of atomic eigenstates in triangular lattice with the largest overlap with the incoming Gaussian mode for various lattice constant and number of atoms (top panels), and transmission, reflection and scattering spectra for different triangular and square lattices (bottom panels). The top graphs shown the collective frequency shift Δ_{Atom} (a), the width Γ_{Atom} (b) and the overlap between the atomic wavefunction $|\Psi_{\text{Atom}}\rangle$ and the profile of the incoming Gaussian beam (c) focused at $z = 0$ with $w_0 = 2.5\lambda_e$. The black dots refer to the most overlapping eigenstate of a triangular lattice with $N = 25^2$ atoms and lattice period $d = 0.87\lambda_e$ having almost zero collective frequency shift $\Delta_{\text{Atom}} = 0.007\Gamma$, small line shape width $\Gamma_{\text{Atom}} = 0.37\Gamma$ and overlap $|\langle\Psi_{\text{Atom}}|\Psi_{\text{Gauss}}\rangle|^2 = 0.4$. The lower graphs show the transmission (blue), reflection (red) and scattering (grey) for two different lattice constants of triangular lattice (d) and (e), and square lattice (f) and (g).

between the atomic wavefunction and the field profile $\simeq 0.4$. To explain this response, we examined atomic eigenstates and we found that the five most mode-matched eigenstates, with total overlap with the bosonic mode ~ 0.99, have almost the same linewidth $\Gamma_{\text{Atom}} \simeq 0.37\Gamma$ and they are almost zero detuned from the atomic frequency ω_e. Hence, we conclude that the incoming field does not couple to a single atomic eigenstate but to a superposition of these five states.

The second row in Fig. 3.4 shows the optical transmission, reflection and scattering versus laser detuning for two cases (d),(e) of triangular lattice, and two cases (f),(g) of square lattice.

Although all of the four cases presented in Fig. 3.4 have large extinction cross section, square lattice with period $d = 0.67\lambda_e$ exhibits nearly perfect reflection into the same Gaussian mode with zero scattering to other modes. Note that the presented results apply to finite but perfect arrays (atoms remain exactly at lattice sites and the arrays are 100% filled), but the performance of the system deteriorates as the density of defects (missing atoms) or atomic position uncertainty (shallow lattice) is increased, which has been verified numerically [8] and experimentally [12].

3.2.2.2 Inhomogeneous atomic arrays

So far we have examined atoms with the same resonant frequency ω_e, but as we show below, by changing slightly the resonance of every atom one can further increase optical cross section of atomic array for incoming Gaussian beams and create focusing lenses using flat atomic arrays. We thus allow a spatial variation of the resonant frequency and thereby the detuning Δ_j for each atom j. Equation (3.5a) is now modified as

$$\left(i\Delta_j - \frac{1}{2}\Gamma\right) b_j - \frac{1}{2}\sum_{j\neq i} F_{ij} b_i = -i\Omega_j e^{i\boldsymbol{k}\cdot\boldsymbol{r}_j}\,, \tag{3.20}$$

and can be solved the same way as before. Different frequency shift can be introduced in each lattice site by applying a non-uniform (space dependent) electric or magnetic fields taking advantage of the Stark or Zeeman effects [31, 32].

To achieve fully destructive interference and cancellation between the incoming field and the field scattered from the atomic array, the two fields must have the same angular distribution in the far-field, the same polarization, and a phase difference $\delta\phi = \pi$. We determined that even in the cases with very low transmission, the two fields might have the same amplitude but their phase difference at $z = 0$ was slightly different from $\pi/2$ and had a Gaussian-like distribution. In order to achieve spatially uniform phase difference, we introduce a Gaussian detuning pattern with each atom having a detuning

$$\frac{\Delta_j^{\mathrm{G}}(x_j, y_j)}{\Gamma} = \alpha - \beta f(x_j, y_j), \tag{3.21}$$

where α is a constant that shifts the transmission deep (or reflection peak), β is a multiplying factor which defines the strength of detuning function $f(x_j, y_j)$, and

$$f(x_j, y_j) = 1 - \exp\left[-\frac{x_j^2 + y_j^2}{(\eta w_0)^2}\right]\,, \tag{3.22}$$

where (x_j, y_j) coordinates of the j-th atom, and η is a fine-tuning degree of freedom. We apply Eq. (3.21) to a triangular lattice of $N = 12^2$ atoms with lattice constant $d = 0.87\lambda_e$, using $\alpha = 6.1 \cdot 10^{-3}$, $\beta = 0.1$ and $\eta = 1.704$, and achieve a reduction of transmission coefficient by three orders of magnitude ($T \sim 10^{-8}$), an increase of reflection, in the same Gaussian mode, close to unity (~ 0.99998), and extinction of scattering into all other modes. Figure 3.5 shows the transmission, reflection and scattering coefficients versus frequency detuning of the above configuration (a) without and (b) with Gaussian detuning pattern. The insets reveal the precise minimum and maximum value of transmission and reflection coefficients, respectively. In another inset we plot the phase $\arg(b_n)$ of each quantum emitter obtained

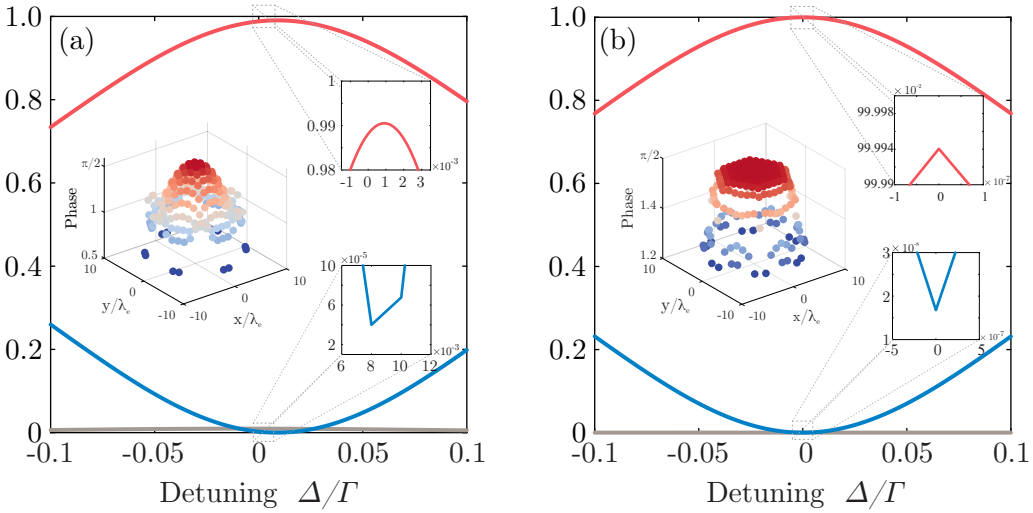

Figure 3.5: Transmission (blue), reflection (red) and scattering (gray) spectra from a triangular lattice of atoms without (a) and with (b) Gaussian detuning pattern given by Eq. (3.21) using the parameters $\alpha = 6.1 \cdot 10^{-3}$, $\beta = 0.1$ and $\eta = 1.704$. Insets in both graphs reveal the minimum and maximum value of transmission and reflection, respectively, and the phase of the amplitude of each atom in steady state driven by resonant light ($\Delta = 0$). Comparing the two graphs becomes clear that Gaussian detuning pattern creates a uniform phase $\pi/2$ in whole array achieving thus almost perfect reflection along with zero transmission and scattering in the far-field. For the chosen set of parameters, the transmission deep and reflection peak are shifted to resonant frequency. In the simulations we used an array of $N = 12^2$ atoms with lattice period $d = 0.87\lambda$ and applied a Gaussian beam with $w_0 = 2.5\lambda_e$.

upon solving the Schödinger equation for resonant light which verifies that we may achieve uniform phase among all quantum emitters equal to $\pi/2$ with the parameters suggested above. The parameters have been chosen to also shift transmission deep and reflection peak to zero detuning. We applied various Gaussian detuning patterns to several configurations and we achieved much better performance than without applying them.

We next consider the possibility of creating focusing lenses and apply parabolic detuning pattern to atomic arrays,

$$\Delta_j^{\mathrm{Par}}(x_j, y_j) = \delta \, \frac{x_j^2 + y_j^2}{\lambda_e^2} \,, \tag{3.23}$$

where δ defines lens strength, in other words larger δ leads to shorter focus distance and smaller beam waist. The array with parabolic pattern radiates a Gaussian beam focused at distance $z_{\mathrm{f}} \leq z_R/2$ and beam waist $\tilde{w}_0 \leq w_0$. In Fig. 3.6 we plot the focused beam waist $\tilde{w}_0$ and the focus distance z_{f} of the Gaussian mode radiated from triangular atomic array. The graphs show that we can both reflect and focus the incoming Gaussian beam, however the tighter we focus the beam the lower is the reflectivity of the array due to the difference between the incoming and dipole radiated fields. The focusing distance achievable in this way is limited by diffraction $z_{\mathrm{f}} \leq z_{\mathrm{R}}/2$, as obtained numerically in Fig. 3.6(b) and analytically proven in [33]. We can put two of such flat arrays with parabolic detuning and create an optical cavity with length $2z_{\mathrm{f}}$. This can be advantageous that these arrays are flat because it is experimentally challenging to place atoms in curved lattices.

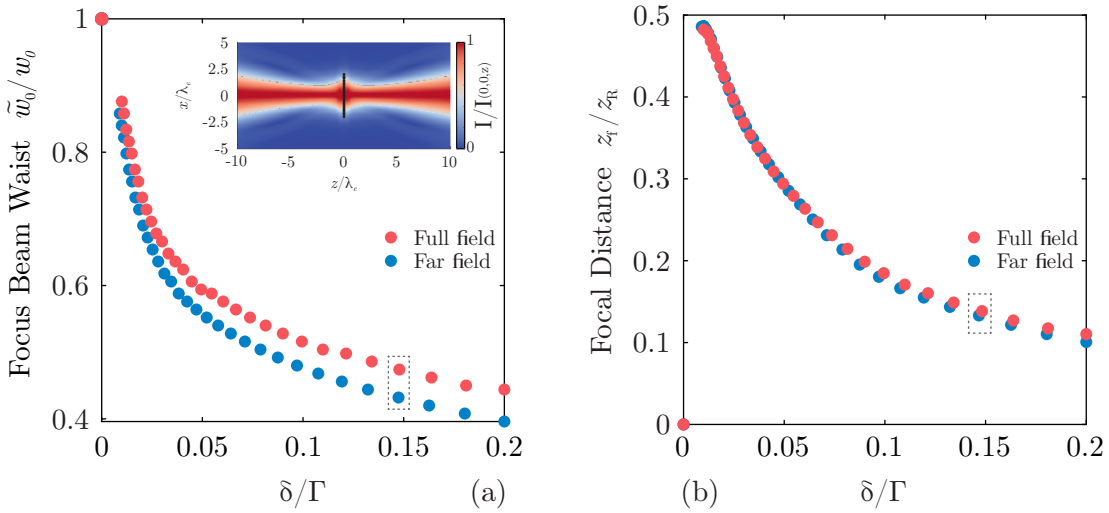

Figure 3.6: Characteristics of a Gaussian beam radiated from triangular array of atoms with parabolic detuning pattern $\Delta_j^{\text{Par}} = \delta(x_j^2 + y_j^2)/\lambda_e$ induced by an incoming Gaussian field with w_0 and z_{R}. In (a) we show the focus beam waist $\tilde{w}_0/w_0$, and in (b) we show the focal distance z_{f}/z_R of the field radiated from the atomic array, calculated using all the field terms (red), and using only the far-field term (blue) revealing a small, expected deviation when beam is tightly focused. The focusing distance achievable in this way is limited by diffraction $z_{\text{f}} \leq z_R/2$, as shown in (b). Inset shows the normalized intensity of the radiated field for $\delta \simeq 0.15\Gamma$, see also data points enclosed in dashed boxes. For the simulation we used triangular lattice with period $d = 0.87\lambda_e$ and $N = 12^2$ atoms driven by a Gaussian mode with waist $w_0 = 2.5\lambda$ at the atomic array.

The next step is to apply two different detuning profiles $\Delta_j^{\pm}(x_j, y_j)$ that can deflect the incoming beam into two different angles $\theta^{\pm}$, see Fig. 3.7(a). Our aim is to determine the detuning profiles $\Delta_n^{\pm}$ and the corresponding radiated fields $\boldsymbol{E}_{\text{dip}}^{\pm}$ resulting in total fields $\boldsymbol{E}_{\text{tot}}^{\pm} = \boldsymbol{E}_{\text{inc}} + \boldsymbol{E}_{\text{dip}}^{\pm}$ that have small overlap, at least in the forward direction. To that end, we apply linear detuning pattern along x-axis

$$\Delta_j^{\pm}(x_j, y_j) = \pm\delta \, \frac{x_j}{d} \,, \tag{3.24}$$

where d is the lattice constant, and δ defines the detuning pattern inclination. Figure 3.7(b) shows the overlap between the angular distributions of the two fields in the far-field, calculated via

$$\xi_{\text{f}} = \frac{\left| \int_{\phi=0}^{2\pi} \int_{\theta=0}^{\pi/2} E_{\text{tot}}^{+} E_{\text{tot}}^{-} \sin\theta \mathrm{d}\theta\mathrm{d}\phi \right|}{\left[\int_{\phi=0}^{2\pi} \int_{\theta=0}^{\pi/2} |E_{\text{tot}}^{+}|^2 \sin\theta \mathrm{d}\theta\mathrm{d}\phi\right]^{1/2} \left[\int_{\phi=0}^{2\pi} \int_{\theta=0}^{\pi/2} |E_{\text{tot}}^{-}|^2 \sin\theta \mathrm{d}\theta\mathrm{d}\phi\right]^{1/2}} \tag{3.25a}$$

$$\xi_{\text{b}} = \frac{\left| \int_{\phi=0}^{2\pi} \int_{\theta=\pi/2}^{2\pi} E_{\text{tot}}^{+} E_{\text{tot}}^{-} \sin\theta \mathrm{d}\theta\mathrm{d}\phi \right|}{\left[\int_{\phi=0}^{2\pi} \int_{\theta=\pi/2}^{2\pi} |E_{\text{tot}}^{+}|^2 \sin\theta \mathrm{d}\theta\mathrm{d}\phi\right]^{1/2} \left[\int_{\phi=0}^{2\pi} \int_{\theta=\pi/2}^{2\pi} |E_{\text{tot}}^{-}|^2 \sin\theta \mathrm{d}\theta\mathrm{d}\phi\right]^{1/2}} \tag{3.25b}$$

in the forward and backward direction, respectively. Figure 3.7(b) reveals that the two linear detunings can lead to two different fields which, however, are not fully distinguishable and

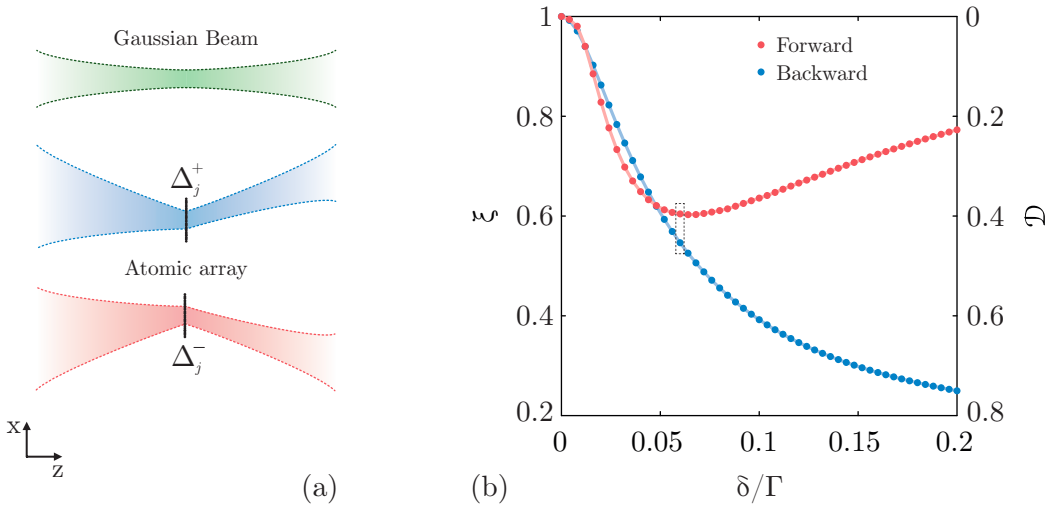

Figure 3.7: (a) Schematic illustration of the incident Gaussian beam (green) without the atomic array, total field created by the incident beam and the atomic array with the detuning pattern Δ_n^+ (blue), and the total field when the detuning pattern Δ_n^- (red). (b) Overlap in the forward (red) and backward (blue) direction between the two total fields created due to incident beam on triangular atomic array with detuning pattern $\Delta_n^\pm$. Right axis shows how distinguishable $\mathcal{D} = 1 - \xi$ the two modes are. For the simulation we used triangular lattice with period $d = 0.87\lambda_e$ and $N = 25^2$ atoms driven by a Gaussian mode with waist $w_0 = 5\lambda_e$ at the atomic array.

their overlap remains finite. The optimal detuning occurs for $\delta = 0.064\Gamma$ where the forward overlap is $\xi_\mathrm{f} = 0.6$ and the backward $\xi_\mathrm{b} = 0.52$. We have tried several detuning profiles, such as cubic, shifted parabolic and spherical, and sawtooth, but have not achieved better distinguishability.

Due to the symmetry of our system, the total power radiated from the atomic array is equally divided between the forward and backward directions which precludes achieving exotic radiation patters. This restriction can be overcome by breaking the symmetry using two or more layers of atoms that create a bilayer or trilayer of atoms [34,35]. We finally note that, as is well known from antenna engineering, one can control the radiation patterns by changing the phases and the amplitudes of every emitter [36,37]. Similarly, Grankin *et al.* [34] and Guimond *et al.* [35] have suggested preparation of single excited states that match the phase front and the amplitude profile of the desired modes.

3.2.3 Pulsed fields

In the previous section we studied atomic arrays driven by a weak continuous-wave field, exhibiting remarkable performance in transmission, reflection and focusing of the incoming beam. Here we show that atomic arrays driven by time-dependent pulsed fields retain these capabilities but with lower efficiency.

We assume a Gaussian wavepacket $\sim \exp(-\frac{t^2}{2\tau^2})$ od duraton τ containing less than one photon on average and solve the time dependent Eqs. (3.4) to calculate the total transmission, reflection and scattering as the integral of their time dependent values. In Fig. 3.8 we plot these coefficients for a triangular lattice of $N = 25^2$ interacting atoms in the pulsed regime,

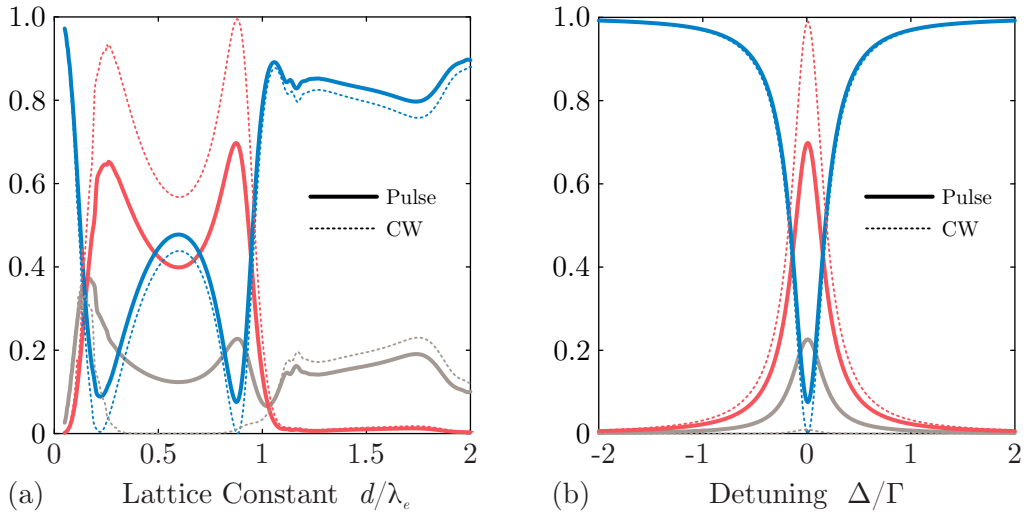

Figure 3.8: Optical power transmission, reflection and scattering of a Gaussian wavepacket through triangular 2D array of $N = 25^2$ interacting atoms. Panel (a) shows the resonant ($\Delta = 0$) transmission (blue), reflection (red) and scattering (grey) coefficients (solid lines) versus lattice constant d of triangular lattice driven by Gaussian wavepacket with duration $\tau = 200/\Gamma$. Panel (b) shows the transmission, reflection and scattering spectra (solid lines) using the same wavepacket on a triangular lattice with constant $d = 0.87\lambda_e$. For comparison, continuous wave results (dashed lines) are plotted in both graphs, revealing that in pulsed scheme transmission and reflection coefficients deteriorate while scattering is mainly enhanced. For the simulations, the incoming Gaussian pulse is $\sim \exp(-\frac{t^2}{2\tau^2})$ and we also assumed Gaussian spatial distribution with waist $w_0 = 2.5\lambda_e$ at the array.

along with the respective coefficients obtained for the continuous wave driving, revealing the lower efficiency in transmission cancellation and reflection into the same mode. Figure 3.8(a) shows that the large atomic array with lattice constant $d = 0.87\lambda_e$ transmits less than 15% and reflects $\sim 65\%$ of the incoming field back to the same mode, while the remaining 20% is scattered to all the other modes. The enhancement of scattering at the expense of reflection and transmission blocking in the pulsed regime, as compared to continuous wave regime, is evident for all the lattice constants. Figure 3.8(b) verifies that for detuning away from atomic resonance atomic arrays driven by pulses behave similarly to continuous wave scheme but with lower efficiency.

In Fig. 3.9 we illustrate the temporal response of an atomic array driven by long and short Gaussian pulses. This figure reveals a finite time response of the atomic arrays to the incoming pulses, which follows from Eqs. (3.3) and should be contrasted with the steady-state solutions for a continuous-wave field. For short pulses, the delayed atomic response reduces further the transmission cancellation and reflection of of the probe pulse and increases the light scattering, since the destructive/constructive interference of the incoming and generated by the atom fields is incomplete. For instance, in Fig. 3.9(a) we obtain total (time integrated) transmission 7.74%, reflection 69.82% and scattering 22.44%, while in Fig. 3.9(b) we have total transmission 22.44%, reflection 35.22% and scattering 42.34%. Another interesting feature shown in Fig. 3.9 is that transmission, reflection and scattering rates are affected by the pulse shape and have in general temporal shapes different from each other and the

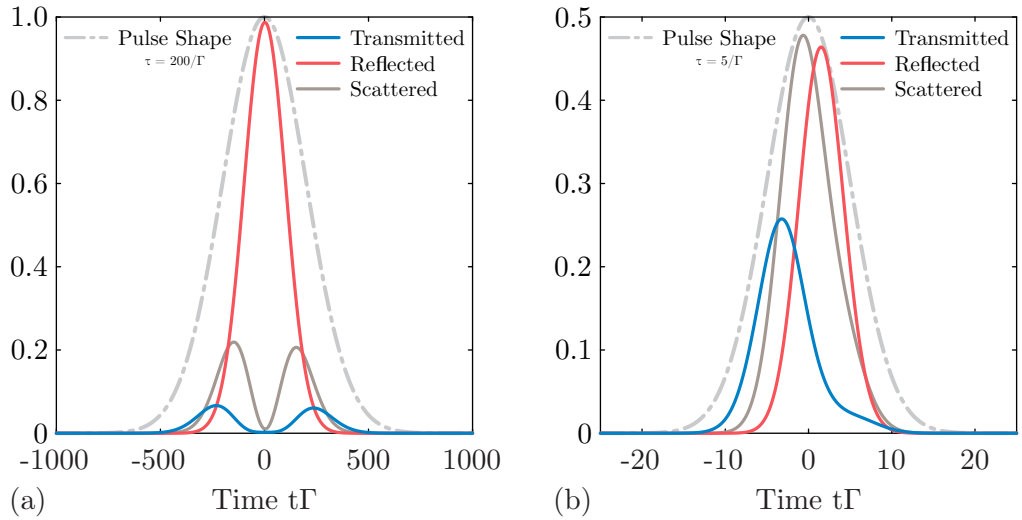

Figure 3.9: Time-dependence of the transmission, reflection and scattering of a Gaussian wavepacket through triangular 2D array of $N = 25^2$ interacting atoms with period $d = 0.87\lambda_e$ for Gaussian input pulses of duration $\tau = 200/\Gamma$ (a) and $\tau = 5/\Gamma$ (b). Shorter incoming pulses lead to delayed atomic response resulting in more scattering and transmission.

incoming pulse shape, especially for shorter pulses in the transient regime when the system does not have sufficient time to follow the steady-state response. We conclude that short pulses are mainly scattered and reflected, while longer pulses asymptotically approach the continuous wave regime. The main characteristics mentioned above remained for all the types of pulses we have investigated, namely: *sech, renctangular, Lorentzian* and *sinc*.

Chapter 4

Multiple Excitations

In this chapter we consider small ensembles of closely–spaced atoms driven by strong coherent laser radiation, and allow multiple excitations of the atomic ensembles. Unlike the previous chapter, we do not truncate the Hilbert space of the system to a single or a few excitation subspace, which permits us to examine the nonlinear regime of the cooperative atom–light interaction. We make use of QSW Monte–Carlo approach to study superradiant and subradiant emission of the photons and calculate their correlations revealing non-classical light radiation, such as photon bunching and antibunching. First, we explore the radiation properties of a driven pair of atoms along with anlytical treatment. Then we examine the radiation properties of three atoms considering various geometries of the atomic positions.

4.1 Pair of atoms

Consider two closely–spaced atoms, with interatomic distance $r_{12} \ll \lambda_e$, driven by a laser field with wave vector $\boldsymbol{k}_c$ and resonant frequency $\omega_c \sim \omega_{eg}$. The coupling strength of the laser field $\mathcal{E}$ with the pair of atoms is expressed by its Rabi frequencies Ω_+ on the transisitions $|gg\rangle \longrightarrow |+\rangle$ and $|+\rangle \longrightarrow |ee\rangle$, and $\pm\Omega_-$ on the transitions $|gg\rangle \longrightarrow |-\rangle$ and $|-\rangle \longrightarrow |ee\rangle$, respectively. These Rabi frequencies are given by

$$\Omega_\pm = \frac{\Omega}{\sqrt{2}} \left(1 \pm e^{-\boldsymbol{k}\cdot\boldsymbol{r}_{12}}\right) , \tag{4.1}$$

where $\Omega = \wp\mathcal{E}/\hbar$ is the Rabi frequency of the field for a single isolated atom. Hence, in the limit of small interatomic distances we can approximate Eq. (4.1) as

$$\Omega_+ \simeq \sqrt{2}\Omega \,, \tag{4.2a}$$

$$\Omega_- \simeq i\sqrt{2}\Omega\zeta\cos(\phi) \,, \tag{4.2b}$$

where $\zeta = kr_{12}$ is the dimensionless distance and ϕ is the angle between vectors $\boldsymbol{k}$ and $\boldsymbol{r}_{12}$. Thus, in the case of the driving field propagating perpendicular to the interatomic axis, $\boldsymbol{k}\perp\boldsymbol{r}_{12}$, Ω_- vanishes, while in the case of the field propagating parallel to the interatomic axis, $\boldsymbol{k}||\boldsymbol{r}_{12}$, Ω_- is maximized with $\zeta \ll 1$. In physical terms, the subradiant $|gg\rangle \longrightarrow |-\rangle$ transition exhibits a *quadrupolar* behavior and dipole-moment suppression, due to destructive interference of the two-atom interactions with the field, as opposed to their constructive interference in the superradiant $|gg\rangle \longrightarrow |+\rangle$ transition [38].

Consider a plane wave propagating with wave vector $\boldsymbol{k}\perp\boldsymbol{r}_{12}$ where the antisymmetric path

is forbidden and the symmetric path is driven with Rabi frequency $\Omega_+ = \sqrt{2}\Omega$. We thus have a three level system in ladder (Ξ) configuration with levels $|gg\rangle, |e+g\rangle, |ee\rangle$. We can get a feeling of how this three-level system behaves by solving the Schrödinger equation using the effective Hamiltonian. The amplitude equations, in the rotating frame, are given by [13]

$$\dot{c}_{gg} = i\Omega_1^* c_+ \,, \tag{4.3a}$$

$$\dot{c}_+ = (i\Delta_1 - \gamma_+)c_+ + i\Omega_1 c_{gg} + i\Omega_2^* c_{ee} \,, \tag{4.3b}$$

$$\dot{c}_{ee} = [i(\Delta_1 + \Delta_2) - \gamma_{ee}]c_{ee} + i\Omega_2 c_+ \,, \tag{4.3c}$$

where we simplified the notation for the symmetric state $|+\rangle \equiv |e+g\rangle$, $\Delta_1 = \omega_c - \omega_{+gg}$ and $\Delta_2 = \omega_c - \omega_{+ee}$ are the detunings of the field from the corresponding atomic transitions, $\Omega_1 = \Omega_2 = \sqrt{2}\Omega$ are the Rabi frequencies of each transition, and $\gamma_+ = (\Gamma + \Gamma_{12})/2$ and $\gamma_{ee} = \Gamma$ are the relaxation (decay) rates of every state. Assuming that intermediate state $|+\rangle$ is not initially populated, $c_+(0) = 0$, we can write Eq. (4.3b) in the integral form as

$$c_+(t) = i\int_0^t \mathrm{d}t' e^{(i\Delta_1 - \gamma_+)(t'-t)}\big[\Omega_1(t')c_{gg}(t') + \Omega_2^*(t')c_{ee}(t')\big] \,. \tag{4.4}$$

If the Rabi frequencies $\Omega_{1,2}$ are smaller than $|\Delta_{1,2}|$ the amplitudes $c_{gg}(t')$ and $c_{ee}(t')$ will not change much while the exponent in Eq. (4.4) experiences many oscillations [13]. Another reasonable assumption is the sufficiently slow change in time of Rabi frequencies $\Omega_{1,2}$, so that they fulfill the condition $|\dot{\Omega}_i/\Omega_i| \ll \Delta_i$ for all $t' \in [0,t]$, the terms in the square brackets of Eq. (4.4) shall be evaluated at $t = t'$ and taken out of the integral [13]. The integration can then be performed, and for times $t \gg 1/\gamma_+$ we obtain the approximate expression

$$c_+(t) = -\frac{\Omega_1 c_{gg} + \Omega_2^* c_{ee}}{\Delta_1 + i\gamma_+} \,. \tag{4.5}$$

Substituting Eq. (4.5) into Eq. (4.3a,c) for the amplitudes c_{gg} and c_{ee} we have

$$\dot{c}_{gg} = -i\frac{|\Omega_1|^2}{\Delta_1 + i\gamma_+}c_{gg} - i\frac{\Omega_1^*\Omega_2^*}{\Delta_1 + i\gamma_+}c_{ee} \,, \tag{4.6a}$$

$$\dot{c}_{ee} = i\Big(\Delta_1 + \Delta_2 - \frac{|\Omega_2|^2}{\Delta_1 + i\gamma_+} - \gamma_{ee}\Big)c_{ee} - i\frac{\Omega_2\Omega_1}{\Delta + \gamma_+}c_{gg} \,. \tag{4.6b}$$

Thus we have performed an adiabatic elimination of the intermediate excited state $|+\rangle$, obtaining coupled differential equations for the amplitudes of states $|gg\rangle$ and $|ee\rangle$. When $|\Delta_1 + \Delta_2| \ll |\Delta_{1,2}|$ and $|\Delta_{1,2}| \gg \gamma_+, |\Omega_{1,2}|$ Eqs. (4.6) reduce to

$$\dot{c}_{gg} = -iZ_{gg}c_{gg} + i\Omega_{\mathrm{eff}}^* c_{ee} \,, \tag{4.7a}$$

$$\dot{c}_{ee} = -\big[i(Z_{ee} - \Delta_1 - \Delta_2) + \gamma_{ee}\big]c_{ee} + i\Omega_{\mathrm{eff}}c_{gg} \,, \tag{4.7b}$$

where $Z_{gg} = |\Omega_1|^2/\Delta_1$ and $Z_{ee} = |\Omega_2|^2/\Delta_1$ are the ac Stark shifts of levels $|gg\rangle$ and $|ee\rangle$, and $\Omega_{\mathrm{eff}} = ie^{i\mathrm{atan}(\Delta_1/\gamma_+)}\Omega_1\Omega_2/\Delta_1 \simeq -i\Omega_1\Omega_2/\Delta_1$ is the effective two-photon Rabi frequency for the transition $|gg\rangle \longrightarrow |ee\rangle$. We may shift the zero point energy of the system via applying the transformation $c_{gg,ee} \to c_{gg,ee}e^{-iZ_{gg}t}$ and obtain

$$\dot{c}_{gg} = i\Omega_{\mathrm{eff}}^* c_{ee} \,, \tag{4.8a}$$

$$\dot{c}_{ee} = (i\Delta_{\mathrm{eff}} - \gamma_{ee})c_{ee} + i\Omega_{\mathrm{eff}}c_{gg} \,, \tag{4.8b}$$

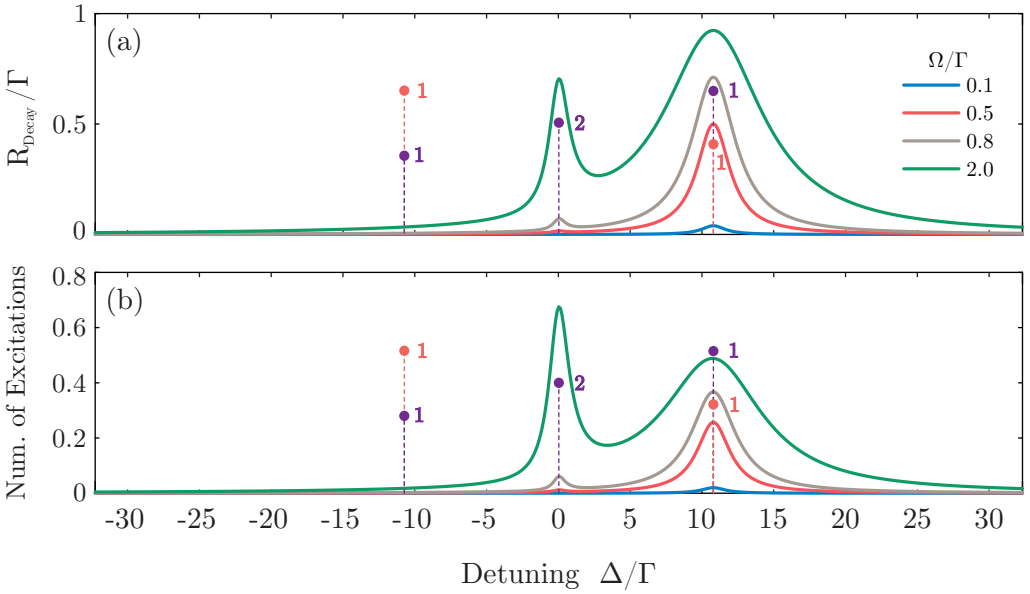

Figure 4.1: Steady state emission rate and excitation spectra of a pair of atoms with normalized interatomic distance $kr_{12} = 0.4$ along the x-axis driven by linearly polarized continuous wave light with wave vector $\boldsymbol{k} \perp \boldsymbol{r}_{12}$ with polarization $\hat{\mathbf{e}} = \hat{\boldsymbol{z}}$. (a) Emission rates for various strengths of the incident field versus frequency detuning. (b) Number of excitations for different incident fields, versus frequency. Graphs show that the pair of atoms can emit and absorb photons only at resonance $\Delta = 0$ (double excited state) and at frequency equal to symmetric collective shift $\Delta = \Delta_{12}$ (single excited symmetric state). When the driving field is detuned by $\Delta = \Delta_{12}$ symmetric state is mainly populated emitting photons two times faster compared to an isolated atom, revealing thus its superradiant behavior. Vertical dashed lines show the transition frequencies between states in the frame rotating with the atomic resonant frequency ω_e, the number next to them shows the number of photons needed for each transition and the color denotes transitions that include ground state $|gg\rangle$ (dark purple) and transitions that include double excited state $|ee\rangle$ (light red). The height of vertical lines does not contain information.

where $\Delta_{\text{eff}} = Z_{gg} - Z_{ee} - (\Delta_1 + \Delta_2)$ the effective two-photon detuning, which in our case reduces to $\Delta_{\text{eff}} = 0$ when the driving field is resonant $\Delta = 0$. Equations (4.8) refer to an effective two-level two-photon transition model that admits analytical solution using the density matrix formulation. We will return to these results and use them to explain some features of the system.

Let us first examine the atomic decay rate and the number of excitations in the system. The decay rate is defined as

$$R_{\text{Decay}} = \sum_{n=1}^{N} \gamma_n \langle \hat{S}_n^\dagger \hat{S}_n \rangle \ , \tag{4.9}$$

while the number of excitations is given by

$$N_e = \sum_{j=1}^{N} \langle \hat{\sigma}_j^\dagger \hat{\sigma}_j \rangle \ . \tag{4.10}$$

Recall that γ_n are the collective decay rates defined in Eq. (2.47) and $\hat{S}_n$ are the collective jump operators defined in Eq. (2.48). In Fig. 4.1 we show the emission rate and the mean number of excitations vs frequency of the excitation laser for a pair of atoms with dimensionless interatomic distance $k_e \boldsymbol{r}_{12} = 0.4\hat{\boldsymbol{x}}$ driven by linearly polarized $\hat{\mathbf{e}} = \hat{\boldsymbol{z}}$ plane wave propagating along $\boldsymbol{k}||\hat{\boldsymbol{y}}$. These graphs reveal that perpendicularly driven pair of atoms cannot absorb or emit photons through the antisymmetric state, which is now shifted to $\Delta = -\Delta_{12} = 10.77\Gamma$. The only way the antisymmetric state can be populated is via a spontaneous quantum jump of the double excited state, but this probability is small and is given by $(\Gamma - \Gamma_{12})/\Gamma \simeq 0.01$. Furthermore, when the incident field is resonant with the singly excited symmetric state ($\Delta = \Delta_{12}$) the atomic system can be excited to this state and then decay two times faster than an isolated two-level atom. For instance, an incoming field with Rabi frequency $\Omega = 0.5\Gamma$ can populate the single excited symmetric state $|e + g\rangle$ with probability 0.25 (Fig. 4.1(b) red line), and due to superradiant character this state will decay to the ground state $|gg\rangle$ with rate $R \sim 0.5\Gamma$ which is two times faster than for the two-level atom. Another interesting point shown in Fig. 4.1 is the ability to populate the double excited state by a two-photon processes. We can partially populate the double excited state by climbing up the state ladder using the intermediate single excited symmetric state. To achieve this, we must shine resonant light ($\Delta = 0$) and apply strong enough Rabi frequency to have the two-photon Rabi frequency $\Omega_{\text{eff}} \sim \gamma_{ee}$. Obviously, in a steady state the symmetric state is also weakly excited leading to slightly higher emission rate than the case of double excited independent atoms.

We are also interested in the statistics of the emitted photons and especially the correlations between them because they can reveal whether the system radiates classical, chaotic or non-classical light. To that end, we use the second order correlation function, assuming a stationary radiated field [39]

$$\mathrm{g}^{(2)}(\tau) = \frac{\langle \hat{E}^\dagger(0)\hat{E}^\dagger(\tau)\hat{E}(\tau)\hat{E}(0)\rangle}{\langle \hat{E}^\dagger \hat{E}\rangle^2} = \frac{\langle \hat{a}^\dagger(0)\hat{a}^\dagger(\tau)\hat{a}(\tau)\hat{a}(0)\rangle}{\langle \hat{a}^\dagger \hat{a}\rangle^2}\,, \tag{4.11}$$

where τ is the time delay between two photon arrivals (or two clicks in the detectors), and $\hat{a}^\dagger\,, \hat{a}$ are the radiated bosonic creation and annihilation operators, respectively. This function quantifies the probability of detecting two photons with time delay τ between them. Equation (4.11) gives $\mathrm{g}^{(2)}(\tau)$ in terms of bosonic field operators, however in our problem a photon is emitted when a quantum jump occurs and thus we can write $\mathrm{g}^{(2)}(\tau)$ in terms of the atomic operators

$$\mathrm{g}^{(2)}(\tau) = \frac{\sum_{mn} \gamma_m \gamma_n \langle \hat{S}_m^\dagger(0)\hat{S}_n^\dagger(\tau)\hat{S}_n(\tau)\hat{S}_m(0)\rangle}{|\sum_n \gamma_n \langle \hat{S}_n^\dagger \hat{S}_n\rangle|^2}\,, \tag{4.12}$$

where the denominator is analogous to the square of the radiated intensity. We calculate the second order correlation function from many realizations of quantum trajectories using the QSW Monte–Carlo technique of Section 2.2, and associating quantum jumps with radiated photons. Note that in the case of photon emission by N independent two level systems the photon-photon correlation at $\tau = 0$ are

$$\mathrm{g}^2(0) = \frac{N}{N+1}, \tag{4.13}$$

and obviously $\mathrm{g}^{(2)}(0) = 0$ when $N = 1$.

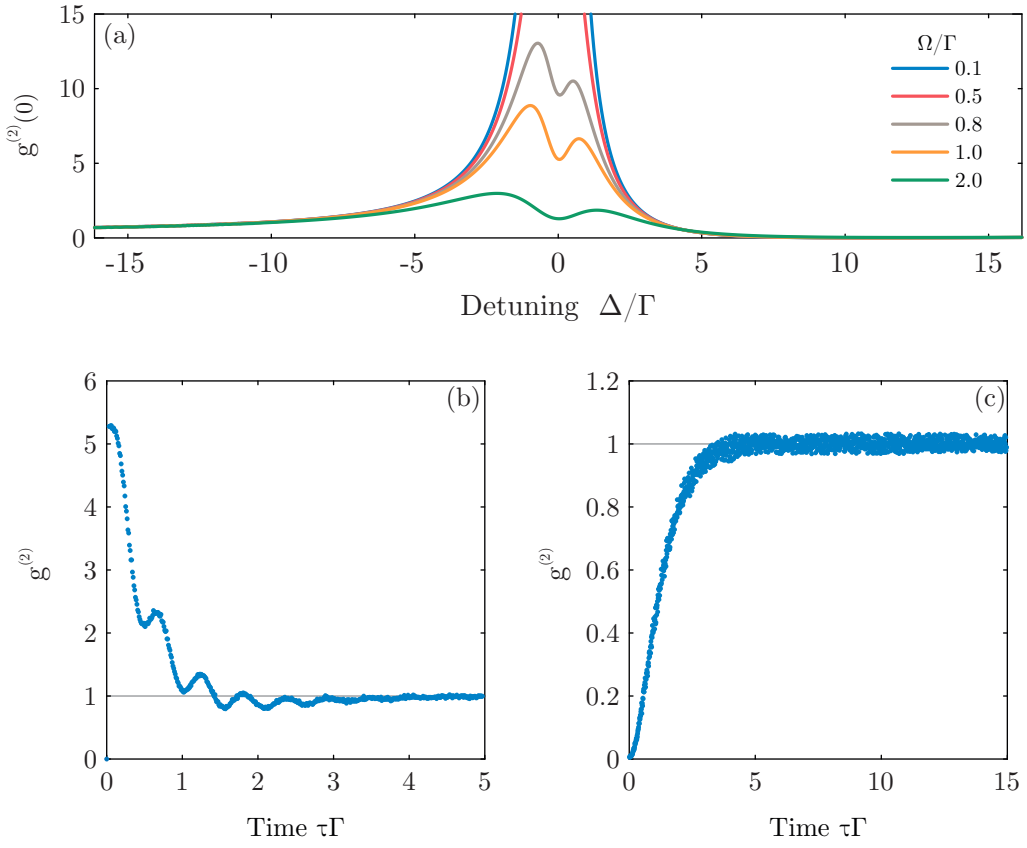

Figure 4.2: Second order correlation function of photons radiated by a pair of atoms with normalized interatomic distance $kr_{12} = 0.4$ driven by linearly polarized continuous wave light with wave vector $\boldsymbol{k} \perp \boldsymbol{r}_{12}$. (a) Second order correlation function for zero time delay $g^{(2)}(\tau = 0)$ vs the excitation laser frequency for various Rabi frequencies Ω. (b) Second order correlation function versus time delay τ for Rabi frequency $\Omega = \Gamma$ and detuning $\Delta = 0$. (c) Same as (b) with $\Omega = \Gamma/5$ but detuning $\Delta = \Delta_{12} = 10.77\Gamma$. Results plotted in (b) and (c) were averaged over $M = 8000$ realizations with the system evolved till times $t_{\text{end}} = 3000/\Gamma$. Simulation parameters are identical with the previous figure.

In Fig. 4.2 we show the correlation function of the photons emitted by a perpendicularly driven pair of atoms with interatomic distance $kr_{12} = 0.4$. Figure 4.2(a) reveals that $g^{(2)}(0)$ has larger values when the atomic system is driven close to resonance $\Delta = 0$, which means that the atoms mainly radiate non-classical highly bunched photon pairs. For instance, for a weak Rabi frequency $\Omega = 0.1\Gamma$ we obtain $g^{(2)}(0) \simeq 100$. This can be understood by looking at Fig. 4.1(b) where the emission rate in the weak driving regime is close to zero resulting to even smaller denominator in Eq. (4.12). Moreover, for weak Rabi frequencies $g^{(2)}(0)$ has one peak at $\Delta = 0$, however when the Rabi frequency becomes stronger the initial peak splits into two unequal peaks which shift away from $\Delta = 0$ as Ω increases, creating thus a local deep at two-photon resonant frequency.

To examine further the correlations of the emitted photons we calculate and plot $g^{(2)}(\tau)$ in Fig.4.2(b),(c). We now find that for $\Delta = 0$ and $\Omega = 1\Gamma$, the pair of atoms radiates bunched photons whose correlation exhibit oscillations and extends up to $\tau \simeq 2/\Gamma$. The graph reveals

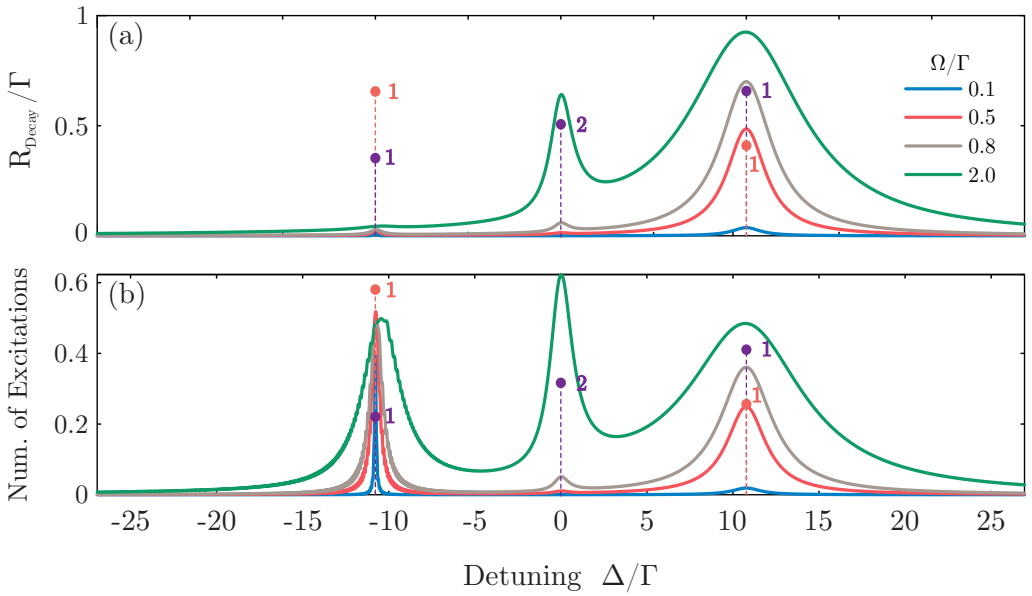

Figure 4.3: Steady state emission rate and excitation spectra of a pair of atoms with normalized interatomic distance $kr_{12} = 0.4$ driven by linearly polarized continuous wave light with wave vector $\boldsymbol{k}||\boldsymbol{r}_{12}$. (a) Emission rate versus detuning for various Rabi frequencies of the incident field. (b) Number of excitations versus detuning for different Rabi frequencies. Graphs show that for parallel driving the atomic pair can emit and absorb photons at resonance $\Delta = 0$ (double excited state), at frequency equal to symmetric collective shift $\Delta = \Delta_{12}$, and at frequency equal to antisymmetric collective shift $\Delta = -\Delta_{12}$. When the driving field is detuned by $\Delta = -\Delta_{12}$ the antisymmetric state is mainly populated while emitting very few photons compared to an isolated atom, revealing thus its subradiant behavior. Vertical dashed lines are the same with those in Fig. 4.1. In the simulation, atoms were placed on x-axis and the field was propagating along x-axis with polarization $\hat{\mathbf{e}} = \hat{\boldsymbol{z}}$.

the high possibility of detecting two photons almost together, $g^{(2)}(0) \simeq 5 > 1$, and that there are times $\tau > 0$ at which the possibility of detecting the second photon peaks. The oscillation period is equal to time needed for the transitions $|gg\rangle \longrightarrow |e+g\rangle$ and $|e+g\rangle \longrightarrow |ee\rangle$, namely

$$\overline{T} = \frac{\pi}{\overline{\Omega}_+} = \frac{\pi}{\sqrt{|\Omega_+|^2 + |\Delta_{12}/2|^2}}\,, \tag{4.14}$$

which in our case results in $\overline{T} = 0.56/\Gamma$. Looking back to the two-level two-photon scheme we understand that the first photon is emitted by the double excited state, then due to superradiant single excited state the system has high probability of emitting a second photon almost instantly after the first one. However, the atomic system may not jump right after the first jump, the second jump may occur when the double excited state is again populated, which leads to spontaneous decay at delays $\tau = q\overline{T}$ with $q = 1, 2, 3, ...$ On the other hand, when the laser field is resonant with the symmetric single photon transition $|gg\rangle \longrightarrow |e+g\rangle$, with $\Omega = \Gamma/5$, we obtain a correlation function similar to a driven isolated atom which can emit only one photon at a time and has to wait until excited state becomes populated again. This is still a non-classical photon source emitting anti-bunched single photons, $g^{(2)}(0) \leq 1$.

We also consider the case when the incident plane wave field propagates parallel to inter-

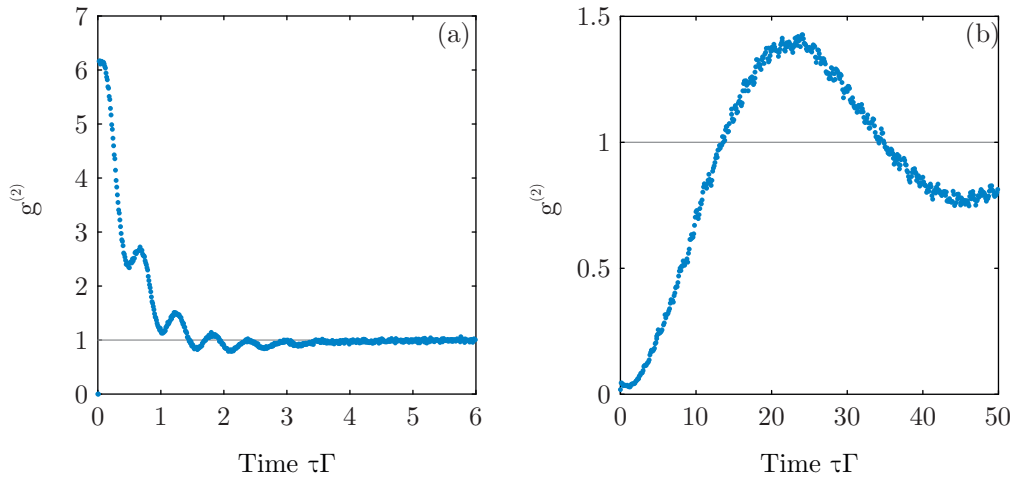

Figure 4.4: Second order correlation function of photons radiated by a pair of atoms with normalized interatomic distance $kr_{12} = 0.4$ driven by linearly polarized continuous wave light with wave vector $\boldsymbol{k}||\boldsymbol{r}_{12}$. (a) second order correlation function versus time delay τ for Raby frequency $\Omega = \Gamma$ and detuning $\Delta = 0$. (b) same with (a) with $\Omega = \Gamma/2$ and detuning $\Delta = -\Delta_{12} = -10.77\Gamma$. Results plotted in (a) and (b) were averaged over $M = 10000$ realizations where the system evolved for times $t_{\text{end}} = 5000/\Gamma$. Simulation parameters are identical to the previous figure.

atomic distance vector $\boldsymbol{r}_{12}$ and show how the pair of atoms behaves in this case. According to Eq. (4.1) the coupling strength between the ground state and the antisymmetric state is non-zero $|\Omega_-| = 0.28|\Omega|$, thus we expect a different behavior compared to the perpendicular case. In Fig. 4.3 we plot the emission spectra and the mean excitation number for various Rabi frequencies. The spectra for the decay rates are similar to those for the perpendicular scheme in Fig. 4.1(a), with small changes due to smaller Rabi frequency Ω_+. For weak Rabi frequency the emission spectra exhibit a small bump at frequency $\Delta = -\Delta_{12}$ due to the excitation of the subradiant state, but when the Rabi frequency is large that bump is buried under the tail of the emission caused by the double excited state. Looking at the excitation spectra we see a third peak located precisely at the transition frequency between the ground state $|gg\rangle$ and the single excited subradiant state $|e-g\rangle$. Due to its subradiant character, this state has very small line width, and it can be populated or even saturated by very weak Rabi frequencies, while the population at this state will jump to ground state very rarely since $\gamma_- \simeq 0.01\Gamma$. However, due to its weak coupling with the incoming field the system need much longer time to reach a steady state. This is attested by the oscillations around the subradiant peak in Fig.4.3(b) that reveal that the system did not reach the steady state, although we let the system propagate for time $t_{\text{end}} = 400/\Gamma$. Finally, this subradiant state is an almost *Dark* state, which can used as a quantum memory for storing one photon for much longer times (two orders of magnitude) compared to a conventional two-level system.

Regarding the photon statistics in the parallel scheme, we found that $g^{(2)}(0)$ is similar to the perpendicular driving, which was expected because the only new feature was the ability to excite the antisymmetric state that results in weak single photon emission. Figure 4.4 shows the correlaion function of the radiated photons for (a) laser resonant with the two-photon transition, and (b) laser resonant with the transition $|gg\rangle \longrightarrow |e-g\rangle$ with $\Delta = -\Delta_{12}$. The

double excited state is excited mainly via the symmetric superradiant state due to its larger coupling strength compared to antisymmetric state, leading to a similar $g^{(2)}(\tau)$ with the perpendicular driving. The system still radiates photon pairs with zero time delay between them, $g^{(2)}(0) = 6.1$. The oscillations have period $\overline{T} = 0.57/\Gamma$ and have the same explanation as those in Fig. 4.2(b). On the other hand, when the incident laser resonantly excites the antisymmetric state the system emits only one photon at a time. Figure 4.4(b) reveals that the system behaves as a slowly-driven slowly-decaying two-level atom with $g^{(2)}(0) \simeq 0$, in other words the system radiates antibunched photons. Due to the combination of weak Rabi frequency Ω_- and small decay rate γ_- of the subradiant state, $g^{(2)}(\tau)$ oscillates with period $\overline{T} = 44/\Gamma$ and the emitted photons remain correlated for long times $\sim 100/\Gamma$.

4.2 Three atoms

We now investigate the response of three atoms driven by a coherent laser. Although we just add one more atom, the system becomes richer and much more complicated. Other than the larger Hilbert space and the increase in the possible transitions, the most important feature is that the non-Hermitian effective Hamiltonian $\mathcal{H}_{\text{eff}}$ in Eq. (2.50a) does not have the same right-eigenvectors with matrix Γ_{ij} in Eq. (2.47), as it used to have in the case of two atoms. In other words, no matter in what state the system is, eigenstate or superposition of eigenstates, when a quantum jump occurs the system will be projected to a superposition of all the eigenstates with one less excitation.

4.2.1 Chain configuration

We begin by solving the eigenvalue problem $\mathcal{H}_{\text{eff}} |\Psi\rangle = \hbar\lambda_n |\Psi\rangle$ which results in 2^3 generally nonorthogonal right-eigenstates with complex eigenvalues λ_{qp}, where q denotes the number of excitations and p is an index to distinguish the states . The real part of each eigenvalue $\mathfrak{Re}\{\lambda_{qp}\} = \delta_{qp}$ determines the level shift δ_{qp} of the corresponding eigenstate from the single-atom resonance ω_e, while the imaginary part $\mathfrak{Im}\{\lambda_{qp}\} = -\tilde{\gamma}_{qp}$ yields the level width or (half-)decay rate $\tilde{\gamma}_{qp}$ of the eigenstate.

In Fig. 4.5 we plot the eigenvalues for three identical atoms placed in 1D lattice with

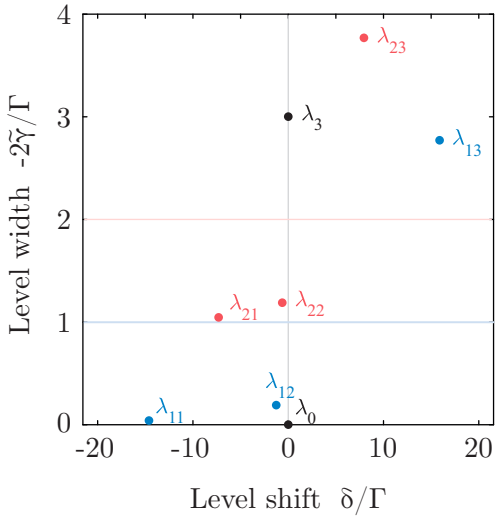

Figure 4.5: Eigenvalues of the effective Hamiltonian $\mathcal{H}_{\text{eff}}$, Eq. (2.50a), for $N = 3$ linearly polarized $\boldsymbol{\wp}||\hat{\boldsymbol{z}}$ atoms placed in a 1D lattice with distance $k\boldsymbol{d} = 0.4\hat{\boldsymbol{x}}$. Each eigenvalue $\lambda_{qp} = (\omega_e + \delta_{qp}) - i\tilde{\gamma}_{qp}$ is shown as a dot at the corresponding coordinates $(\delta_{qp}\,, -2\tilde{\gamma}_{qp})$. Eigenvalues with zero or three excitations are plotted in black color, with one excitation in blue, and those with two excitations are plotted in red. Horizontal lines are plotted to indicate whether an eigenstate is superradiant or subradiant for the corresponding number of excitations.

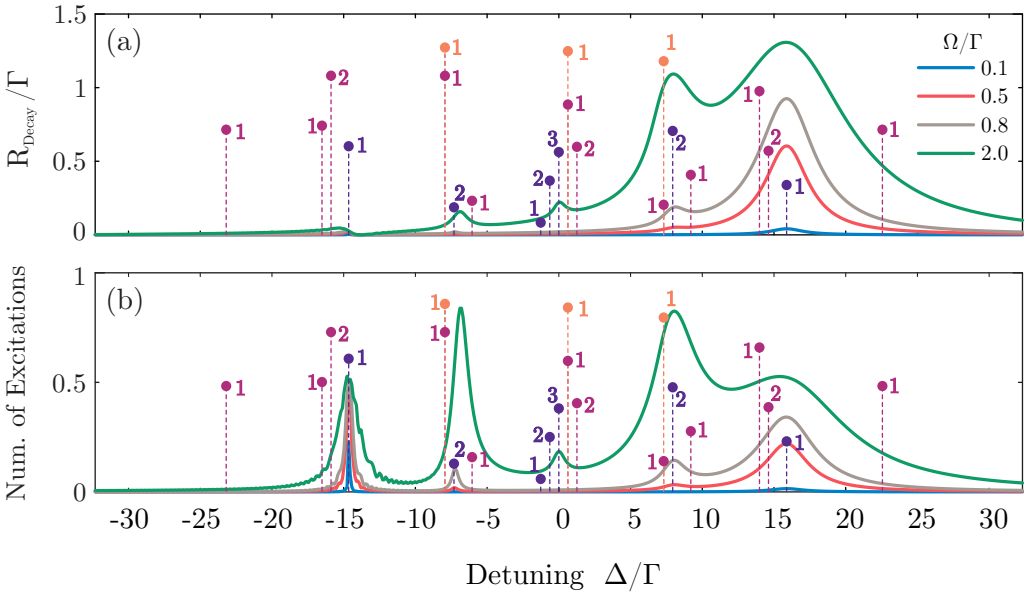

Figure 4.6: Steady state emission rate and excitation spectra of a chain of $N = 3$ atoms with the interatomic period $k\boldsymbol{d} = 0.4\hat{\boldsymbol{x}}$ driven by linearly polarized $\hat{\boldsymbol{e}}||\hat{\boldsymbol{z}}$ continuous wave light with wave vector $\boldsymbol{k}||\hat{\boldsymbol{y}}$. (a) Spectra of the emission rates for various incident fields versus the detuning of the driving laser. (b) Number of excitations for various incident field versus detuning. Vertical dashed lines show the transition frequencies between states in frame rotating with the atomic resonant frequency ω_e, the number next to them shows the number of photons needed for each transition and the color denotes transitions that include ground state (dark purple), transitions that include single excited states (dark red), and those which include double excited states (orange). The height of lines does not contain information.

lattice constant $k\boldsymbol{d} = 0.4\hat{\boldsymbol{x}}$ with linear dipole moment $\wp||\hat{\boldsymbol{z}}$, where we obtain the ground (λ_0) and the triple (λ_3) excited states along with single (λ_{1p}) and double (λ_{2p}) excited superradiant and subradiant eigenstates. Eigenstates with one and two excitations are two subradiant and one superradiant in each case. In general, level shifts δ_{qp} can have any values but the level widths $-2\tilde{\gamma}_{qp}$ must be non-negative, and they must also satisfy the following formula

$$\sum_p -\frac{2\tilde{\gamma}_{qp}}{\Gamma} = qW(N-q)\,, \tag{4.15}$$

where $W(n_g)$ is the number of eigenstates with q excitations, see Eq. (2.17). For instance, for single excited states we have $0 \leq -2\tilde{\gamma}_{1p}/\Gamma \leq 3$ and for triple excited states $0 \leq -2\tilde{\gamma}_{2p}/\Gamma \leq 6$.

Figure 4.6 shows the steady state emission spectra and the excitations in the system for various Rabi frequencies Ω and detunings Δ. In the same figure, we use vertical lines to show the frequencies of all the possible transitions, while we also mark each transition with the corresponding number of photons. Figure 4.6(a) shows that when the driving field is resonant with the single excited superradiant state $|\lambda_{13}\rangle$ ($\Delta \simeq 15\Gamma$) the atomic system emits photons almost three times faster than a conventional two-level system. The same graphs also reveal that the incoming laser can excite a single excited and a double excited subradiant state at detunings $\Delta = -15\Gamma$ and $\Delta = -7.5\Gamma$, respectively. The laser couples to the subradiant state $|\lambda_{11}\rangle$ directly and it can drive the system up and down without radiating

any photons. However, in the case of the double excited subradiant state $|\lambda_{21}\rangle$ the laser drives the state through the intermediate state $|\lambda_{13}\rangle$. For strong Rabi frequencies we can put more excitations in the system but due to the decay rate of $|\lambda_{21}\rangle$ the system radiates stronger than the single excited subradiant state. Another interesting feature is the inability to climb up the excitation ladder and populate the triple excited state, for which there are two reasons. First, the perpendicularly incident plane wave has zero overlap with the antisymmetric subradiant states $|\lambda_{12}\rangle$ and $|\lambda_{22}\rangle$, hence the system cannot climb up through these states. Second, the other way is to take advantage of the strong coupling of superradiant states $|\lambda_{13}\rangle$ and $|\lambda_{23}\rangle$ with the driving field and overcome the frequency difference using strong Rabi frequency. However, even in this case we system has to climb through two superradiant states, which leads to very low population in the triple excited state.

In Fig. 4.7 we plot the second order correlation function for an incoming laser resonant with the transition $|\lambda_0\rangle \longrightarrow |\lambda_{21}\rangle$ with single atom Rabi frequency $\Omega = 0.8\Gamma$. $g^{(2)}(\tau)$ reveals that the system exhibits photon bunching and fast oscillations which means that the second photon arrives mainly after certain time delays. Hence, the first photon is radiated due to the atomic jump from $|\lambda_{21}\rangle$ to a superposition of $|\lambda_{11}\rangle$ and $|\lambda_{13}\rangle$, then the second photon is radiated when the last state jumps to the ground state. The fast beatings occur with frequency equal to the frequency difference between states $|\lambda_{11}\rangle$ and $|\lambda_{13}\rangle$, when these two states interfere constructively $g^{(2)}$ exhibits large values and when they interfere destructively $g^{(2)}$ exhibits much lower values. These beatings decay rapidly because the state $|\lambda_{13}\rangle$ is sperradiant. The slower oscillations that survive for times $\sim 50/\Gamma$ can be attributed to the transition between the ground $|\lambda_0\rangle$ and the subradiant $|\lambda_{11}\rangle$ states.

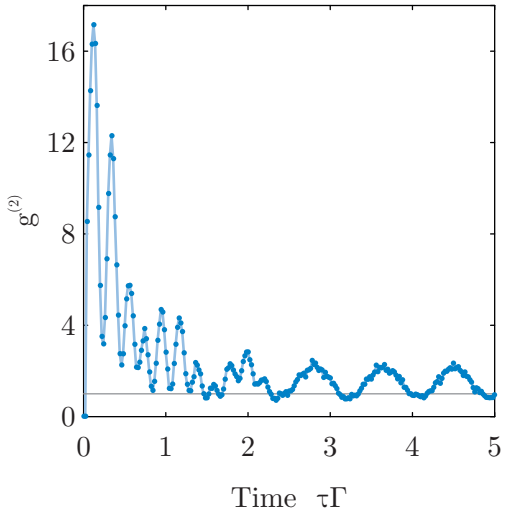

Figure 4.7: Second order correlation function of photons radiated by a chain of $N = 3$ atoms with normalized distance $k\boldsymbol{d} = 0.4\hat{\boldsymbol{x}}$ driven by linearly polarized $\hat{\boldsymbol{e}}||\hat{\boldsymbol{z}}$ continuous wave light with wave vector $\boldsymbol{k}||\hat{\boldsymbol{y}}$. The incoming laser excites the transition $|\lambda_0\rangle \longrightarrow |\lambda_{21}\rangle$ with Rabi frequency $\Omega = 0.8\Gamma$. We averaged over $M = 10000$ realizations with the system evolving for times $t_{\text{end}} = 4000/\Gamma$.

4.2.2 Triangle configuration

We finally consider $N = 3$ atoms in an equilateral triangular configuration with side distance $kd = 0.4$ placed in xz-plane. Again, we assume a a uniform driving laser with linear polarization $\boldsymbol{\wp}||\hat{\boldsymbol{z}}$ and wave vector $\boldsymbol{k}||\hat{\boldsymbol{y}}$. We diagonalize the effective Hamiltonian and plot the eigenvalues λ_{qp} in Fig. 4.8. Although all the interatomic distances are the same, the dipole-dipole interaction is also affected by $|\hat{\boldsymbol{\wp}} \cdot \hat{\boldsymbol{r}}_{ij}|^2$, see Eqs. (2.11), which leads to different

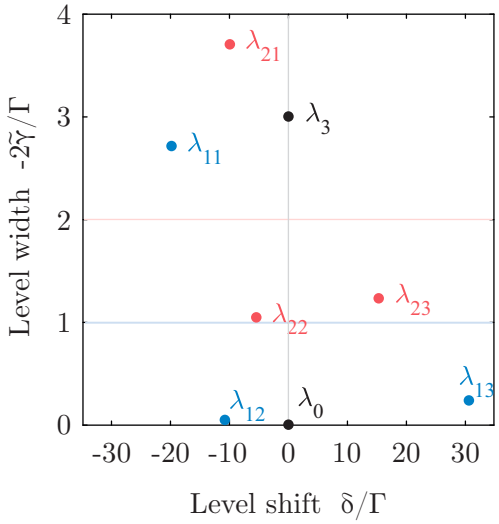

Figure 4.8: Eigenvalues of the effective Hamiltonian $\mathcal{H}_{\text{eff}}$, Eq. (2.50a), for $N = 3$ linearly polarized $\boldsymbol{\wp}||\hat{\boldsymbol{z}}$ atoms placed in equilateral triangular configuration in xz-plane with side distance $d = 0.4$. Each eigenvalue $\lambda_{qp} = (\omega_e + \delta_{qp}) - i\tilde{\gamma}_{qp}$ is shown as a dot at the corresponding coordinates $(\delta_{qp}\,, -2\tilde{\gamma}_{qp})$. Eigenvalues with zero and three excitations are plotted with black color, one excitation with blue, and those with two excitations with red. Horizontal lines help to distinguishing whether an eigenstate is superradiant or subradiant.

interactions between the two atoms placed on x-axis and the atom placed on z-axis.[1] Due to small interatomic distances we obtain one superradiant and two subradiant states at single and double excitation level, the eigenvalue spectrum is similar to the chain configuration but not the same.

In Fig. 4.9 we plot the emission rate spectra and the excitations of the triangular atomic configuration perpendicularly driven with various Rabi frequencies Ω. We see a dominant peak in the emission graph which is attributed to the single excited superradiant $|\lambda_{11}\rangle$ shifted by $\Delta = -20\Gamma$. The dominant peak in the excitation graph occurs when the laser drives the transitions $|\lambda_0\rangle \longrightarrow |\lambda_{21}\rangle$ and $|\lambda_0\rangle \longrightarrow |\lambda_{12}\rangle$, with the former responsible for the large decay rate while the latter traps the population increasing the excitation number. Furthermore, driving lasers with positive detunings $\Delta = 15\Gamma$ and $\Delta = 30\Gamma$ can excite the subradiant state $|\lambda_{23}\rangle$ and $|\lambda_{13}\rangle$, respectively. Eigenstate $|\lambda_{23}\rangle$ can be excited only with strong incoming laser and store more that one excitation. Eigenstate $|\lambda_{13}\rangle$ can be excited with weaker lasers and achieve lower steady state population.

Finally, in Fig. 4.10 we plot $\mathrm{g}^{(2)}(\tau)$ for the two-photon transition $|\lambda_0\rangle \longrightarrow |\lambda_{23}\rangle$ driven with Rabi frequency $\Omega = 0.8\Gamma$. We observe the same phenomenon as we did with chain configuration in Fig. 4.7, where the photons come in pairs and have specific time delays between them. The beatings here are much faster due to the larger frequency difference between states $|\lambda_{11}\rangle$ and $|\lambda_{13}\rangle$, while we do not observe slow long lived oscillation due to weak coupling between the laser and $|\lambda_{13}\rangle$.

[1] In the case of circular dipole moment $\hat{\boldsymbol{\wp}} = (\hat{\boldsymbol{x}} \pm i\hat{\boldsymbol{z}})/\sqrt{2}$ the dipole-dipole interaction is only affected by the interatomic distances, because $|\hat{\boldsymbol{\wp}} \cdot \hat{\boldsymbol{r}}_{ij}|^2 = 1\,, \forall \boldsymbol{r}_{ij} \perp \hat{\boldsymbol{y}}$. For an equilateral triangle the effective Hamiltonian has eigenvalue spectrum with a pair of degenerate states at single excitation level and another degenerated pair at double excitation level.

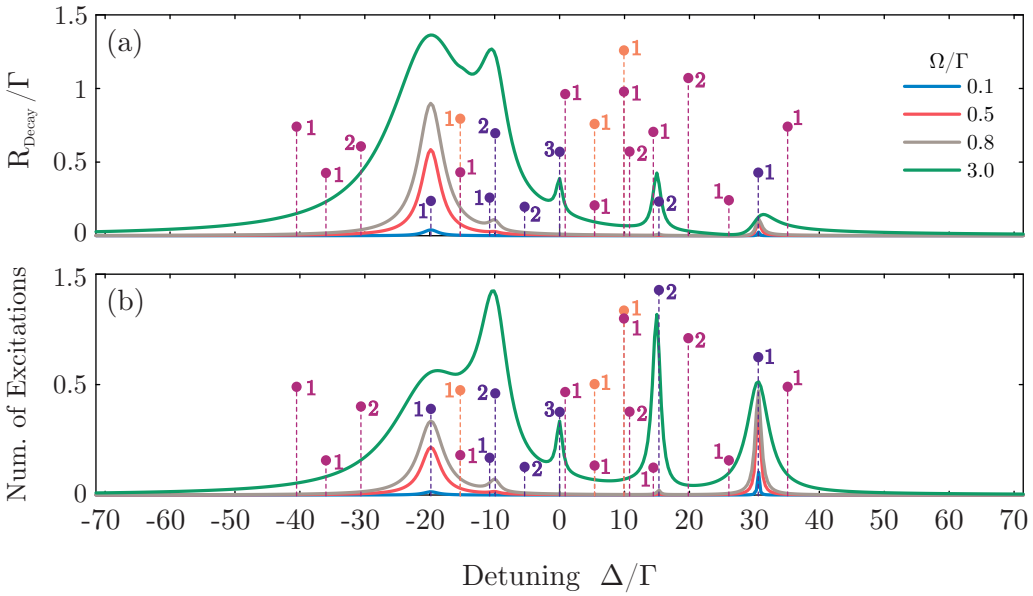

Figure 4.9: Steady state emission rate and excitation spectra of $N = 3$ atoms in equilateral triangular configuration in xz-plane with side distance $kd = 0.4$ driven by linearly polarized $\hat{\boldsymbol{e}}||\hat{\boldsymbol{z}}$ continuous wave light with wave vector $\boldsymbol{k}||\hat{\boldsymbol{y}}$. (a) Emission rate spectra for various incident fields versus detuning of the driving laser. (b) Number of excitations for various incident fields versus detuning. Vertical dashed lines show the transition frequencies between different states in the frame rotating with the atomic resonant frequency ω_e, the number next to them shows the number of photons needed for each transition and the color denotes transitions that include ground state (dark purple), transitions that include single excited states (dark red), and those which include double excited states (orange).

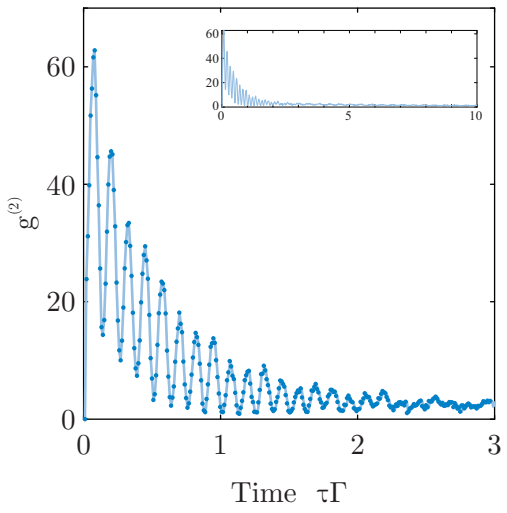

Figure 4.10: Second order correlation function of photons radiated by $N = 3$ atoms with equilateral triangular configuration placed in xz-plane with side distance $kd = 0.4$ driven by linearly polarized $\hat{\boldsymbol{e}}||\hat{\boldsymbol{z}}$ continuous wave light with wave vector $\boldsymbol{k}||\hat{\boldsymbol{y}}$. The incoming laser drives the transition $|\lambda_0\rangle \longrightarrow |\lambda_{23}\rangle$ with Rabi frequency $\Omega = 0.8\Gamma$. We averaged over $M = 10000$ with the system evolving for times $t_{\text{end}} = 4000/\Gamma$.

Chapter 5

Conclusions and Future Extensions

In conclusion, in this thesis we have discussed two topics: (i) the enhanced cross section of atomic arrays under the single excitation approximation, and (ii) the radiation properties of small ensembles of closely-spaced atoms driven by strong coherent laser fields.

For the large atomic arrays we showed that they exhibit enhanced optical cross section when the incident laser field drives a resonant collective atomic eigenstate, or a superposition of eigenstates with similar frequency shifts. We showed that both superradiant and subradiant states can serve as optical mirrors achieving almost zero transmission and perfect reflection of the incoming mode. Furthermore, we suggested to apply inhomogeneous detuning patterns on the atoms to improve the performance of atomic arrays as mirrors, to create parabolic mirrors from flat arrays, and to deflect the incoming laser beam. A future extension in this direction would be the improvement of beam deflection by connecting the detuning pattern with the phase front of a Gaussian mode emitted in the desired direction, or by considering more than one atomic arrays. Given that the experiments with atomic mirrors are conducted with pulsed laser fields [12], it would be interesting to explore further the atomic array response in the pulsed regime and find the optimal pulse characteristics (shape, duration, chirp).

For the case of small ensembles of closely-spaced atoms, we showed that they can be driven by classical coherent light and emit bunched or anti-bunched photons. Long-lived subradiant states can serve as quantum memories to store one or more photons. Moreover, we presented the eigenvalue spectrum showing the large energy shifts between atomic eigenstates which lead to non-linear behavior of the system. For example, we can put one excitation in the system by shining continuous laser on a specific transition, while putting a second excitation in the systems using the same driving field is not possible due to large frequency shifts between the states. An interesting extension here would be to consider more atoms and explore possible quantum protocols that can excite atomic states with desired subradiant characteristics.

Appendix A

Detection of selected mode

Here we present a simple method used in Chap. 3 to study the transmission, reflection and scattering of a Gaussian mode of light by an atomic ensemble [30].

Consider a photodetector, with unit efficiency, that can collect photons from a single mode of radiation field

$$\hat{\boldsymbol{\mathcal{E}}}_{\rm det}(\boldsymbol{r}) = \hat{\mathbf{e}}_{\rm det}\sqrt{\frac{\hbar\omega_d}{2\epsilon_0 AL}}\varphi_{\rm det}(\boldsymbol{r})\hat{a}_{\rm det} \tag{A.1}$$

where $\hat{\mathbf{e}}_{\rm det}$ is the polarization of the mode, $\varphi_{\rm det}(\boldsymbol{r})$ is the spatial distribution, AL is the quantization volume with A being the cross section of the mode and L the quantization length, and $\hat{a}_{\rm det}$ is the annihilation operator for the photons in that mode. We assume that bosonic operators $\hat{a}^\dagger_{\rm det}, \hat{a}_{\rm det}$ satisfy the equation $\langle \hat{a}^\dagger_{\rm det}\hat{a}_{\rm det}\rangle = n_{\rm det} = n\,(L/c)$ with c being the speed of light in free space, which is equivalent to assuming the quantization volume being a hypothetical cavity, with volume $V = AL$, moving with the speed of light. The total field in the selected mode is given by the sum of the incident field and the field radiated by the atoms,

$$\hat{a}_{\rm det} = \hat{a}_{\rm inc;det} + \hat{a}_{\rm atom;det}\,. \tag{A.2}$$

For instance, when the incident mode is the same with the detector mode and the are no atoms we have $\hat{a}_{\rm det} = \hat{a}_{\rm inc;det} \equiv \hat{a}_{\rm inc}$, while in the case where the incoming mode is orthogonal to the detection mode, we have $\hat{a}_{\rm det} = 0$ in the absence of atoms and $\hat{a}_{\rm det} = \hat{a}_{\rm atom;det}$ in the presence of atoms. The number of incident photons in detector mode is calculated by the projection of the total incoming field onto the detector mode. The field radiated by the atoms into the detector mode is given by

$$\hat{a}_{\rm det}(t) = i\sum_{j=1}^{N} g^*_{\rm det}(\boldsymbol{r}_j)\int_0^t {\rm d}t'\hat{\sigma}_j(t')e^{-\omega_d(t-t')}\,, \tag{A.3}$$

which follows from the Heisenberg equation for the field operator

$$\dot{\hat{a}}_{\rm det}(t) = i\sum_{j=1}^{N} g^*_{\rm det}(\boldsymbol{r}_j)\hat{\sigma}_j(t)\,, \tag{A.4}$$

where $g_{\rm det}(\boldsymbol{r}_j) = \sqrt{\hbar\omega_d/(2\epsilon_0 AL)}\,\boldsymbol{\varphi}_{\rm det}(\boldsymbol{r}_j)\cdot\boldsymbol{\wp}_{eg}/\hbar$ is the atom-field coupling strength with

$\boldsymbol{\varphi}_m(\boldsymbol{r}_j) = \varphi_m(\boldsymbol{r}_j)\hat{\mathbf{e}}$. We substitute Eq. (A.4) in Eq. (A.2) and obtain

$$\begin{aligned}\hat{a}_{\text{atom;det}} &= \frac{i}{\hbar}\sqrt{\frac{\hbar\omega_d}{2\epsilon_0 Ac}}\sum_{j=1}^{N}\varphi^*_{\text{det}}(\boldsymbol{r}_j)\hat{\mathbf{e}}^*_{\text{det}}\cdot\wp_{ge}\hat{\sigma}_j = \frac{i}{\hbar}\sqrt{\frac{L}{c}}\sum_{j=1}^{N}\sqrt{\frac{\hbar\omega_d}{2\epsilon_0 AL}}\varphi^*_{\text{det}}(\boldsymbol{r}_j)\hat{\mathbf{e}}^*_{\text{det}}\cdot\wp_{ge}\hat{\sigma}_j \\ &= \frac{i}{\hbar}\sqrt{\frac{L}{c}}\sum_{j=1}^{N}\sqrt{\frac{\hbar\omega_d}{2\epsilon_0 AL}}\varphi^*_{\text{det}}(\boldsymbol{r}_j)\hat{\mathbf{e}}^*_{\text{det}}\cdot\wp_{ge}\hat{\sigma}_j = i\sqrt{\frac{L}{c}}\sum_{j=1}^{N}\frac{\mathcal{E}^*_{\text{det}}(\boldsymbol{r}_j)\hat{\mathbf{e}}\cdot\wp_{ge}}{\hbar}\hat{\sigma}_j \\ &= i\frac{1}{\sqrt{n\frac{c}{L}}}\sum_{j=1}^{N}\frac{\mathcal{E}^*_{\text{det}}(\boldsymbol{r}_j)\hat{\mathbf{e}}\cdot\wp_{ge}\sqrt{n}}{\hbar}\hat{\sigma}_j = i\frac{1}{\sqrt{\langle\hat{a}^\dagger_{\text{inc;det}}\hat{a}_{\text{inc;det}}\rangle}}\sum_{j=1}^{N}\Omega^*_{\text{det}}(\boldsymbol{r}_j)\hat{\sigma}_j\,,\end{aligned} \tag{A.5}$$

where the term outside of the summation has units of $[s]^{1/2}$ while the Rabi frequencies Ω_{det} inside the sum have units of $1/s$. Now we can plug Eq. (A.5) into Eq. (A.2) and calculate the rate of photons in detector mode transmitted in the forward direction

$$T = |\,\langle\hat{a}^\dagger_{\text{det}}\hat{a}_{\text{det}}\rangle\,| = |\,\langle\hat{a}^\dagger_{\text{inc;det}}\hat{a}_{\text{inc;det}}\rangle + \langle\hat{a}^\dagger_{\text{atom;det}}\hat{a}_{\text{atom;det}}\rangle\,|\,, \tag{A.6}$$

the reflected into the same backward mode

$$R = |\,\langle\hat{a}^\dagger_{\text{atom;det}}\hat{a}_{\text{atom;det}}\rangle\,|\,, \tag{A.7}$$

and the scattered $S = 1 - T - R$.

In the case of weak driving, meaning that the incoming field does not saturate the atomic transition $\langle\hat{a}^\dagger_{\text{inc}}\hat{a}_{\text{inc}}\rangle/\Gamma \ll 1$ and there is less than one photon in the quantization volume $\langle\hat{a}^\dagger_{\text{inc}}\hat{a}_{\text{inc}}\rangle\frac{L}{c} < 1$, we can truncate the total Hilbert space to up to one excitation and solve the Schrödinger equation obtaining Eq. (3.3). This results in further simplification of Eqs. (A.5), where operators $\hat{\sigma}_j$ can be replaced by b_j. We choose the quantization length L and photon rate in to the mode $\langle\hat{a}^\dagger_{\text{inc}}\hat{a}_{\text{inc}}\rangle$ so that the above conditions are satisfied.

We apply this method in Chapter 3 assuming the same Gaussian mode for the incident and the detector field. Hence, the spatial distribution of the mode is

$$\varphi_{\text{G}}(\boldsymbol{r}) = \frac{w_0}{w(z)}e^{-\frac{x^2+y^2}{w^2(z)}}e^{i(kz-\text{atan}(z/z_R))}e^{-ik\frac{x^2+y^2}{2R(z)}}\,, \tag{A.8}$$

where $z_{_R} = \pi w_0^2/\lambda_0$, and

$$w^2(z) = w_0^2\left[1+\left(\frac{\lambda_0 z}{\pi w_0^2}\right)^2\right] = w_0^2\left[1+\left(\frac{z}{z_{_R}}\right)^2\right]\,, \tag{A.9a}$$

$$R(z) = z\left[1+\left(\frac{\pi w_0^2}{\lambda_0 z}\right)^2\right] = z\left[1+\left(\frac{z_{_R}}{z}\right)^2\right]\,. \tag{A.9b}$$

Evidently, the cross section is $A = \int_{z=0}|\varphi|^2\text{d}S = \pi w_0^2/2$, and $\Omega_{\text{det}}(\boldsymbol{r}_j)$ in Eq. (A.5) is the Rabi frequency of the incident field used in Eqs. (3.3).

Bibliography

[1] R. H. Dicke, "Coherence in Spontaneous Radiation Processes," *Physical Review*, vol. 93, pp. 99–110, Jan. 1954.

[2] A. Svidzinsky and J.-T. Chang, "Cooperative spontaneous emission as a many-body eigenvalue problem," *Physical Review A*, vol. 77, Apr. 2008.

[3] A. A. Svidzinsky, J.-T. Chang, and M. O. Scully, "Cooperative spontaneous emission of N atoms: Many-body eigenstates, the effect of virtual lamb shift processes, and analogy with radiation of N classical oscillators," *Physical Review A*, vol. 81, May 2010.

[4] D. Petrosyan and K. Mølmer, "Collective emission of photons from dense dipole-dipole interacting atomic ensembles," *Physical Review A*, vol. 103, Feb. 2021.

[5] T. Bienaimé, N. Piovella, and R. Kaiser, "Controlled dicke subradiance from a large cloud of two-level systems," *Physical Review Letters*, vol. 108, Mar. 2012.

[6] W. Guerin, M. O. Araújo, and R. Kaiser, "Subradiance in a large cloud of cold atoms," *Physical Review Letters*, vol. 116, Feb. 2016.

[7] L. Ortiz-Gutiérrez, L. Muñoz-Martínez, D. Barros, J. Morales, R. Moreira, N. Alves, A. Tieco, P. Saldanha, and D. Felinto, "Experimental fock-state superradiance," *Physical Review Letters*, vol. 120, Feb. 2018.

[8] R. J. Bettles, S. A. Gardiner, and C. S. Adams, "Enhanced optical cross section via collective coupling of atomic dipoles in a 2d array," *Physical Review Letters*, vol. 116, Mar. 2016.

[9] E. Shahmoon, D. S. Wild, M. D. Lukin, and S. F. Yelin, "Cooperative resonances in light scattering from two-dimensional atomic arrays," *Physical Review Letters*, vol. 118, Mar. 2017.

[10] A. Asenjo-Garcia, M. Moreno-Cardoner, A. Albrecht, H. Kimble, and D. Chang, "Exponential improvement in photon storage fidelities using subradiance and "selective radiance" in atomic arrays," *Physical Review X*, vol. 7, aug 2017.

[11] G. Facchinetti, S. D. Jenkins, and J. Ruostekoski, "Storing light with subradiant correlations in arrays of atoms," *Physical Review Letters*, vol. 117, Dec. 2016.

[12] J. Rui, D. Wei, A. Rubio-Abadal, S. Hollerith, J. Zeiher, D. M. Stamper-Kurn, C. Gross, and I. Bloch, "A subradiant optical mirror formed by a single structured atomic layer," *Nature*, vol. 583, pp. 369–374, July 2020.

[13] P. Lambropoulos and D. Petrosyan, *Fundamentals of Quantum Optics and Quantum Information*. Springer Berlin Heidelberg, 2007.

[14] V. Weisskopf and E. Wigner, "Berechnung der natürlichen linienbreite auf grund der diracschen lichttheorie," *Zeitschrift für Physik*, vol. 63, pp. 54–73, Jan. 1930.

[15] R. H. Lehmberg, "Radiation from an N-Atom System. I. General Formalism," *Physical Review A*, vol. 2, pp. 883–888, Sept. 1970.

[16] L. Novotny and B. Hecht, *Principles of Nano-Optics*. Cambridge University Press, 2012.

[17] J. D. Jackson, *Classical Electrodynamics*. Nashville, TN: John Wiley & Sons, 3 ed., July 1998.

[18] M. Gross and S. Haroche, "Superradiance: An essay on the theory of collective spontaneous emission," *Phys. Rep.*, vol. 93, pp. 301–396, Dec. 1982.

[19] R. H. Lehmberg, "Transition Operators in Radiative Damping Theory," *Physical Review*, vol. 181, pp. 32–38, May 1969.

[20] R. H. Lehmberg, "Radiation from an N-atom System. II. Spontaneous Emission from a Pair of Atoms," *Physical Review A*, vol. 2, pp. 889–896, Sept. 1970.

[21] T. Richter, "Cooperative spontaneous emission from an initially fully excited system of three identical two-level atoms," *Annalen der Physik*, vol. 495, no. 4-5, pp. 234–261, 1983.

[22] C. W. Gardiner, A. S. Parkins, and P. Zoller, "Wave-function quantum stochastic differential equations and quantum-jump simulation methods," *Physical Review A*, vol. 46, pp. 4363–4381, Oct. 1992.

[23] C. W. Gardiner and P. Zoller, *Quantum noise*. Springer Series in Synergetics, Berlin, Germany: Springer, Dec. 2010.

[24] K. Mølmer, Y. Castin, and J. Dalibard, "Monte carlo wave-function method in quantum optics," *Journal of the Optical Society of America B*, vol. 10, p. 524, Mar. 1993.

[25] M. O. Scully and M. S. Zubairy, *Quantum Optics*. Cambridge, England: Cambridge University Press, Sept. 1997.

[26] M. K. Tey, G. Maslennikov, T. C. H. Liew, S. A. Aljunid, F. Huber, B. Chng, Z. Chen, V. Scarani, and C. Kurtsiefer, "Interfacing light and single atoms with a lens," *New Journal of Physics*, vol. 11, p. 043011, Apr. 2009.

[27] M. Mücke, E. Figueroa, J. Bochmann, C. Hahn, K. Murr, S. Ritter, C. J. Villas-Boas, and G. Rempe, "Electromagnetically induced transparency with single atoms in a cavity," *Nature*, vol. 465, pp. 755–758, May 2010.

[28] J. D. Thompson, T. G. Tiecke, N. P. de Leon, J. Feist, A. V. Akimov, M. Gullans, A. S. Zibrov, V. Vuletić, and M. D. Lukin, "Coupling a single trapped atom to a nanoscale optical cavity," *Science*, vol. 340, pp. 1202–1205, June 2013.

[29] R. J. Bettles, S. A. Gardiner, and C. S. Adams, "Cooperative ordering in lattices of interacting two-level dipoles," *Physical Review A*, vol. 92, Dec. 2015.

[30] M. T. Manzoni, M. Moreno-Cardoner, A. Asenjo-Garcia, J. V. Porto, A. V. Gorshkov, and D. E. Chang, "Optimization of photon storage fidelity in ordered atomic arrays," *New Journal of Physics*, vol. 20, p. 083048, Aug. 2018.

[31] D. Petrosyan, K. Mølmer, J. Fortágh, and M. Saffman, "Microwave to optical conversion with atoms on a superconducting chip," *New Journal of Physics*, vol. 21, p. 073033, July 2019.

[32] M. Kaiser, C. Glaser, L. Y. Ley, J. Grimmel, H. Hattermann, D. Bothner, D. Koelle, R. Kleiner, D. Petrosyan, A. Günther, and J. Fortágh, "Cavity-driven rabi oscillations between rydberg states of atoms trapped on a superconducting atom chip," *Physical Review Research*, vol. 4, Mar. 2022.

[33] S. A. Self, "Focusing of spherical gaussian beams," *Applied Optics*, vol. 22, p. 658, Mar. 1983.

[34] A. Grankin, P. O. Guimond, D. V. Vasilyev, B. Vermersch, and P. Zoller, "Free-space photonic quantum link and chiral quantum optics," *Physical Review A*, vol. 98, Oct. 2018.

[35] P.-O. Guimond, A. Grankin, D. Vasilyev, B. Vermersch, and P. Zoller, "Subradiant bell states in distant atomic arrays," *Physical Review Letters*, vol. 122, Mar. 2019.

[36] S. A. Schelkunoff and H. T. Friis, *Antenna Theory and Practice*. John Wiley & Sons, 1952.

[37] C. A. Balanis, *Antenna theory*. Hoboken, NJ: Wiley-Blackwell, 4 ed., Jan. 2016.

[38] D. Petrosyan and G. Kurizki, "Scalable solid-state quantum processor using subradiant two-atom states," *Physical Review Letters*, vol. 89, Oct. 2002.

[39] R. Loudon, *The quantum theory of light*. London, England: Oxford University Press, 3 ed., Sept. 2000.